

# Batch Localization Based on OFDMA Backscatter

XINYU TONG, Shanghai Jiao Tong University, China  
 FENGYUAN ZHU, Shanghai Jiao Tong University, China  
 YANG WAN, Shanghai Jiao Tong University, China  
 XIAOHUA TIAN, Shanghai Jiao Tong University, China  
 XINBING WANG, Shanghai Jiao Tong University, China

OFDMA Wi-Fi backscatter can significantly improve the communication efficiency and meanwhile maintain ultra-low power consumption; however, the ground-up reworking on the core mechanism of traditional Wi-Fi system revolutionizes the basis of many existing Wi-Fi based mechanisms. In this paper, we explore how localization can be realized based on OFDMA backscatter, where a batch localization mechanism utilizing concurrent communication in the OFDMA backscatter system is proposed. We present a series of mechanisms to deal with the fundamental change of assumptions brought by the new paradigm. First, we process signals at the receiver in a finer granularity for signal classification. Then we remove phase offsets in real time without interrupting the communication. Finally, we propose an extended MUSIC algorithm to improve accuracy with limited localization information in OFDMA backscatter mechanism. We implement a prototype under the 802.11g framework in WARP, based on which we conduct comprehensive experiments to evaluate our proposed mechanism. Results show that our system can localize 48 tags simultaneously, while achieving average localization errors within 0.49m. The tag's power consumption is about 55-81.3 $\mu$ W.

CCS Concepts: • Networks → Location based services.

Additional Key Words and Phrases: OFDMA, localization, concurrency, backscatter

## ACM Reference Format:

Xinyu Tong, Fengyuan Zhu, Yang Wan, Xiaohua Tian, and Xinbing Wang. 2019. Batch Localization Based on OFDMA Backscatter. *Proc. ACM Interact. Mob. Wearable Ubiquitous Technol.* 3, 1, Article 25 (March 2019), 25 pages. <https://doi.org/10.1145/3314412>

## 1 INTRODUCTION

Wi-Fi is widely used in today's Internet-of-things (IoT) applications as the wireless backhaul; however, in order to realize the vision of universal deployment of Wi-Fi based IoT systems, the following two issues have to be well addressed: First, IoT applications are featured by a large number of devices with short bursts of data, while the random access mechanism adopted by the current Wi-Fi network is unable to support concurrent communications among IoT devices, which incurs low communication efficiency; second, most of IoT devices are battery-powered, while the Wi-Fi communication module is power hungry, which incurs the inconvenience of changing the battery.

---

Authors' addresses: Xinyu Tong, Shanghai Jiao Tong University, 800 Dong Chuan Rd, Shanghai, 200240, China, tongxinyu1993@sjtu.edu.cn; Fengyuan Zhu, Shanghai Jiao Tong University, 800 Dong Chuan Rd, Shanghai, 200240, China, jsqdzhfengyuan@sjtu.edu.cn; Yang Wan, Shanghai Jiao Tong University, 800 Dong Chuan Rd, Shanghai, 200240, China, wanyang@sjtu.edu.cn; Xiaohua Tian, Shanghai Jiao Tong University, 800 Dong Chuan Rd, Shanghai, 200240, China, xtian@sjtu.edu.cn; Xinbing Wang, Shanghai Jiao Tong University, 800 Dong Chuan Rd, Shanghai, 200240, China, xwang8@sjtu.edu.cn.

---

Permission to make digital or hard copies of all or part of this work for personal or classroom use is granted without fee provided that copies are not made or distributed for profit or commercial advantage and that copies bear this notice and the full citation on the first page. Copyrights for components of this work owned by others than ACM must be honored. Abstracting with credit is permitted. To copy otherwise, or republish, to post on servers or to redistribute to lists, requires prior specific permission and/or a fee. Request permissions from permissions@acm.org.

© 2019 Association for Computing Machinery.

2474-9567/2019/3-ART25 \$15.00

<https://doi.org/10.1145/3314412>

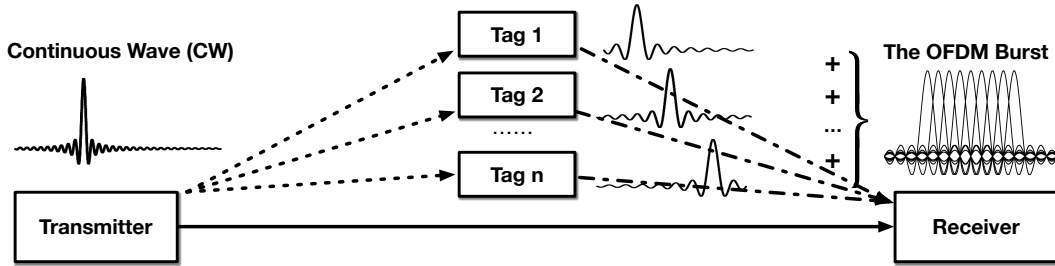


Fig. 1. Wi-Fi OFDMA Backscatter System.

The ongoing evolution of Wi-Fi towards next-generation 802.11ax [1, 3, 10, 28] provides an opportunity to address **issue 1**. 11ax replaces the random access mechanism with orthogonal frequency division multiple access (OFDMA), which can significantly improve communication concurrency. In particular, OFDMA can allocate orthogonal subcarriers to devices, which can then transmit data concurrently due to the orthogonality, instead of transmitting sequentially as under the random access mechanism. Moreover, 11ax optimizes the energy efficiency with the target wait time (TWT) scheme, where the devices transmit only at pre-negotiated time slots with access point (AP) and remain asleep in the rest of the time.

In contrast to the TWT scheme adopting the traditional duty-cycling concept, Wi-Fi backscatter [18, 40, 41] can address **issue 2** by providing a more effective power saving solution, which removes the RF component from the IoT device and utilizes the excitation signal from regular or dedicated transmitters as carriers. Instead of actively generating RF signals, the IoT device is only with digital component thus incurs  $O(\mu W)$  power consumption. However, the reported Wi-Fi backscatter systems [18, 40, 41] still adopt the random access mechanism in the MAC layer, and the IoT devices have to perform backscatter communication sequentially.

OFDMA backscatter combines the benefits of high concurrency in OFDMA and ultra-low power consumption in backscatter, which is a promising technology for ubiquitous deployment of IoT devices in the future. The architecture of OFDMA backscatter system is illustrated in Fig. 1. The transmitter generates continuous wave (CW) and also performs control and management functions; the backscatter devices (tags) shift frequency of the CW to frequency bands of orthogonal subcarriers, modulate the local information and then backscatter the modulated CW to the receiver. The backscattered signals will be synthesized into complete OFDM bursts at the receiver and then decoded. We implement and comprehensively evaluate the system, and the results show that the system can support 48 tags to transmit concurrently, with  $O(\mu W)$  power consumption.

While promising for large-scale IoT applications requiring ultra-low power consumption, OFDMA backscatter paradigm revolutionizes the basis of many works based on traditional Wi-Fi platform, among which Wi-Fi localization can serve as an outstanding case study. Applying existing Wi-Fi localization mechanisms to OFDMA Wi-Fi backscatter platform is confronted with the following challenges: First, existing Wi-Fi localization techniques [19, 29] based on Intel 5300 tool kit [14] leverage channel state information (CSI) from the single transmitter; however, CSI observed by the receiver as shown in Fig. 1 is the combined information from two different line-of-sight (LoS) paths at least, i.e. TX-RX and Tags-RX, which makes it more challenging for signal classification. Second, the phase offset calibration [8, 12, 35] that is necessary for CSI localization requires to interrupt the communication, which hinders concurrent communication among IoT tags. Third, current CSI localization [9, 19, 20, 36] needs information of redundant subcarriers from a single transmitter, but high concurrency in OFDMA backscatter prefers each tag using a single OFDMA subcarrier.

In this paper, we propose a batch localization mechanism based on OFDMA backscatter. Particularly, our mechanism can concurrently localize at least 48 tags in batch, in contrast to existing designs [9, 19, 20, 36]

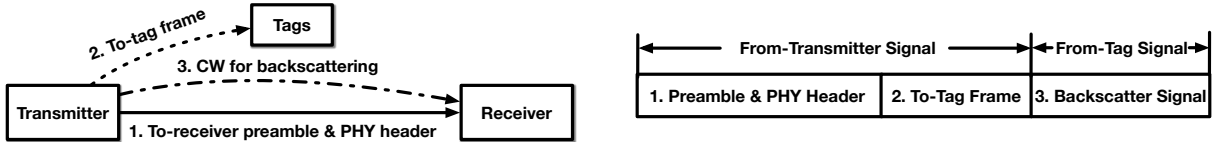


Fig. 2. Synchronization Mechanism in Wi-Fi OFDMA Backscatter.

utilizing multiple subcarriers to localize a single device. The scheme could significantly improves the localization efficiency, and especially useful for large-scale IoT applications such as inventory and smart factory, where there could be a large number of battery-powered sensors needs localization service in real time. Moreover, our proposed mechanism maintains the ultra-low power consumption of OFDMA backscatter devices and incurs no interruptions to regular communication functions. Our technical contributions are two-fold:

First, we for the first time present the design of the concurrent localization system based on OFDMA backscatter (**§Section 3**). In particular, we develop the OFDM burst processing scheme to separate multi-tag signals for concurrent CSI collection, where different subcarriers can be utilized to localize corresponding backscatter tags (**§Section 4**). We utilize CSI with respect to different antennas and different propagation paths to realize automatic phase offset elimination, which not only provides accurate AoA measurement but also eliminate redundant packet transmission for phase offset calibration in existing work [12, 35] (**§Section 5**). Since limited subcarrier allocation for each tag leads to lower accuracy, we finally extend traditional MUSIC algorithm by establishing the virtual antenna array and thus improve the accuracy of AoA calculation (**§Section 6**). We finally obtain AoAs with respect to different transceivers and realize concurrent localization (**§Section 7**).

Second, we implement a prototype of concurrent localization under the 802.11g framework in WARP, based on which we conduct comprehensive experiments to evaluate our propose mechanism. results show that our system can achieve average localization errors within  $0.49m$  while the tag consumes  $55\text{-}81.3\mu W$  active power. Further, our system achieves  $50\times$  valid concurrency compared with existing systems.

## 2 PRELIMINARIES

### 2.1 OFDMA Backscatter System

We implement concurrent localization based on Wi-Fi OFDMA backscatter systems [42], thus we first highlight the OFDMA backscatter system, so that the following contents of this paper can be understood.

Wi-Fi backscatter provides a more effective power saving solution for low-power IoT devices. The first Wi-Fi backscatter system in 802.11b framework is proposed in passive Wi-Fi [18], where the authors realize  $11Mbps$  transmission with  $59.2\mu W$  energy consumption. The key design of Wi-Fi backscatter is the frequency shifting mechanism in tags, where the tag shifts ambient wireless signals from one channel to another channel. Since backscatter systems can realize frequency shifting operation without the energy-consuming RF component, they enable low-power communication.

In contrast to Wi-Fi backscatter in 802.11b framework, Wi-Fi OFDMA backscatter enhances system concurrency and capacity. The crux of any OFDMA system is the effective synchronization mechanism. To synchronize the OFDMA backscatter system, there are three parts in OFDMA backscatter designs as shown in Fig. 2. First, the 802.11g preamble and PHY header are transmitted to synchronize the clock of transmitter and receiver; Second, excitation signal transmitters produce to-tag frame to synchronize tags and the transmitter. Since the transmitter and receiver have been synchronized in the first part, we can synchronize the whole system; Third, the transmitter broadcasts continuous wave (CW) that would be backscattered to different subcarriers by tags. Based on three steps in Fig. 2, we can coordinate the frequency shift in multiple tags as shown in Fig. 1, which is equivalent to

assign different subcarriers to different tags. In this way, backscatter signals coming from multiple tags make up a completed OFDM signal that could be demodulated at the receiver.

## 2.2 Challenges

Since the lack of strict synchronization mechanism makes OFDMA backscatter unfeasible, the synchronization designs mentioned above are necessary. However, such a mechanism brings three new challenges to concurrent localization. This section introduces particular challenges in batch localization systems, so that readers could focus on certain sections in the following discussions.

*Challenge 1: Collecting Feasible CSI.* Existing localization techniques [19–21, 29] localize the target based on CSI collected by Intel 5300 tool kit [14] which derives 30 CSI measurements for 64 subcarriers from each packet. To distinguish this kind of CSI from the CSI collected in our system, we define the CSI collected by Intel 5300 tool kit as **packet-level CSI**. In the OFDMA backscatter system, as shown in Fig. 2, signals observed by the receiver is the combined information from many paths. For example, if 48 tags are employed in the system, the receiver would observe the combined information across 49 different propagation paths which consist of 48 Tags-RX paths and one TX-RX path. The combination of signals can be observed in symbol domain and frequency domain, where symbol domain represents different OFDM symbols in the OFDM burst and frequency domain means different OFDMA subcarriers. In symbol domain, one OFDM burst contains both from-transmitter and from-tag signals as shown in Fig. 2. Since Intel 5300 tool kit derives packet-level CSI based on the preamble [13, 14] that exactly comes from the transmitter instead of tags, packet-level CSI cannot be utilized to localize tags. In frequency domain, one OFDM burst contains backscatter signals of multiple tags as shown in Fig. 1. Since packet-level CSI can only provide 30 measurements, it cannot be utilized to classify 48 different tags. Therefore, instead of utilizing existing packet-level CSI directly, it is necessary to process received signals in a finer granularity for the path classification. Only in this way, we can derive feasible CSI for target localization.

*Challenge 2: Eliminating Phase Offsets.* As verified in previous experiments [21], phase offsets severely affect localization performance. In particular, uncalibrated phase offsets would lead to an average 60 degrees error of AoA calculation, which is not feasible in localization systems. To address *challenge 1*, we derive fine-grained CSI of each OFDM symbol. However, in contrast to packet-level CSI, our fine-grained CSI suffers even more from phase offsets which consist of continuous dynamic phase offset and down conversion phase offset. **Continuous dynamic phase offset** could be addressed via the method introduced in [23], we thus focus on discussing why it is challenging to remove the second type of phase offset without dedicated packet transmission. In particular, **down conversion phase offset** is caused by the down conversion step at the receiver. To address this challenge, it is necessary for prior works [8, 12, 35] to perform phase offset calibration which requires to interrupt the communication. In particular, ArrayTrack [35] utilizes RF cables to manually measure this phase offset. Since down conversion phase offset would be reset as a new random value once device initializes, the manual RF cable calibration is not practical. Meanwhile, Phaser and AWL [8, 12] require special calibration communication between transceivers, which inevitably interrupts normal communication of the tag. When there are a large number of tags in OFDMA backscatter systems as shown in Fig. 1, such a calibration scheme means massive interruptions of communication. Therefore, it is necessary to design a scheme to calibrate or remove down conversion phase offset without interrupting the communication, which hasn't been realized by any existing work.

*Challenge 3: Localizing with Limited Information.* Caused by OFDMA backscatter mechanisms, limited subcarriers could be assigned to each tag. It is because in OFDMA backscatter systems, multiple subcarriers are assigned to different tags. Since the amount of subcarriers is constant, with the increase of concurrently localized tags, the number of subcarriers assigned to each tag decreases. In fact, such a design makes prior localization systems

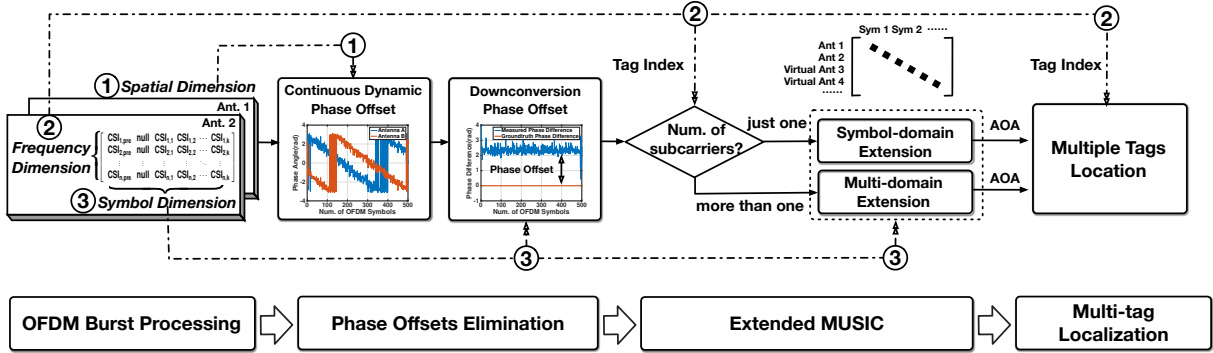


Fig. 3. System Overview.

depending on the information of redundant subcarriers unfeasible. For example, RF-Echo [9] and WiTag [20] derive ToF based on CSI of multiple subcarriers. When OFDMA backscatter systems assign each tag only a single subcarrier for high concurrency, these systems cannot provide satisfying solution. Another possible scheme against limited subcarriers is sending massive packets for more CSI measurements [19]. However, frequent communication is energy-consuming and cannot be satisfied in practical low-power systems. Since a single CSI measurement is exactly unstable and therefore leads to inaccurate AoA measurements, this challenge is necessary to be addressed in the batch localization system. However, high concurrency mechanisms limit the employment of redundant subcarriers while low-power communication mechanisms make continuous massive packets inoperable. Thus, it is challenging to localize targets accurately with extremely limited information.

### 3 SYSTEM OVERVIEW

Our system can localize multiple backscatter tags concurrently, which consists of the following four modules shown in Fig. 3 to address the three challenges mentioned above.

*OFDM Burst Processing Module.* As discussed in *challenge 1*, each OFDM symbol contains CSI corresponding to multiple paths. In particular, the signals of different subcarriers usually come from different tags as shown in Fig. 1. In addition, each subcarrier signal consists of the from-transmitter part and the from-tag part as shown in Fig. 2. In this module, we process the OFDM burst and derives CSI based on three different dimensions, i.e., spatial dimension, frequency dimension and symbol dimension. Among them, ***spatial-dimension CSI*** labeled with ① represents CSI at different antennas, and it could be utilized to remove continuous dynamic phase offset. ***Frequency-dimension CSI*** labeled with ② means CSI across different subcarriers, and it could be employed to separate multi-tag signals for concurrent localization. ***Symbol-dimension CSI*** labeled with ③ means CSI of different OFDM symbols, and it could be utilized to remove down conversion phase offset (*challenge 2*) and realize our extended MUSIC scheme (*challenge 3*).

*Phase Offsets Elimination Module.* As described in *challenge 2*, we must remove phase offsets to enable AoA measurement. In this module, we utilize spatial-dimension and symbol-dimension CSI to remove these two phase offsets respectively. We first remove dynamic continuous phase offset based on spatial-dimension CSI as shown in [23]. Secondly, the basic idea of down conversion phase offset elimination is that we can observe the same phase offset across different propagation paths. Since symbol-dimension consists of both from-transmitter and from-tag CSI respectively depicting the channel state of different propagation paths, we can therefore remove down conversion phase offset. In contrast to previous methods, we for the first time remove phase offsets without

dedicated packet transmission, which is more important with the rapid rise of connectivity needs from IoT devices. Besides, since our phase offset elimination module works in real time, extra performance evaluation and re-calibration processes proposed in previous work [12] are also not necessary.

*Extended MUSIC Scheme Module.* Since limited subcarriers can be allocated to each tag and there are usually 2 ~ 3 antennas equipped in COTS devices, we can hardly derive accurate AoA for localization (*challenge 3*). To address this challenge, we proposed extended MUSIC scheme consisting of ***symbol-domain extension*** and ***multi-domain extension***. As shown in Fig. 3, we first determine the number of subcarriers assigned to the localized tag and then perform corresponding extended MUSIC scheme. Symbol-domain extension and multi-domain extension share the same basic idea, i.e., improving performance by establishing the virtual antenna array. Mathematically, we extend the dimensions of traditional MUSIC matrix to enable more accurate AoA measurements. In particular, the OFDM burst processing module provides us with the fine-grained channel state depiction and about 500× samples of 500 OFDM symbols compared with packet-level CSI. Therefore, we can utilize symbol-dimension information to extend MUSIC matrix for AoA measurements. Meanwhile, when more than one subcarriers assigned, we can also employ both symbol-dimension and frequency-dimension information to further extend MUSIC matrix for more accurate results.

*Multi-tag Localization Module.* To localize backscatter tags, it is necessary to derive at least two AoAs with respect to different transceivers. In multi-tag localization module, we combine AoAs relative to different transceivers and then localize the tag. Since backscatter tags can always be indexed by corresponding subcarriers, we can derive multi-tag position based on frequency-dimension information.

## 4 OFDM BURST PROCESSING

In this section, we describe in detail how we process the OFDM burst for feasible CSI collection to address *challenge 1*. For this purpose, we first analyze advantages of our finer-grained CSI and then show how to derive it in our system. Since the finer-grained CSI consists of three different dimensions, i.e. spatial dimension, frequency dimension and symbol dimension, we define it as ***three-dimension CSI (3D-CSI)*** in the following contents of this paper.

### 4.1 3D-CSI Analysis

Compared with previous works [9, 12, 19, 20, 35, 36] which employ multiple antennas, subcarriers and packets for pure performance improvement, we explore the nature of different kinds of CSI and design a more practical localization system. What we concern in our system are concurrency, energy conservation, communication compatibility and accuracy. *Concurrency* represents that we can simultaneously localize multiple tags. Without concurrent mechanisms, we must schedule multiple tags in sequence to derive feasible CSI [41], which is considered to be inefficient [7, 16, 17]. *Energy conservation* represents that we don't require continuous massive packets for accurate localization due to inconsistency between continuous massive packets and low-power designs. Meanwhile, compared with single-packet localization, massive-packet localization will lead to lower efficiency. *Communication compatibility* means that we cannot interrupt other devices' communication while localizing certain targets or calibrating phase offsets. It is because communication interruption will become more and more insufferable with the increase of connected IoT devices. *Accuracy* means we can derive accurate target position, which is obviously important for any localization system. Now we discuss different CSI dimensions as follows:

The spatial dimension represents CSI at different antennas. One function of spatial-dimension CSI is to calculate AoA and then localize multiple tags. As shown in many prior works [8, 12, 19, 29, 35], the antenna array is essential infrastructure for AoA localization. In addition, spatial-dimension CSI could also be employed to ensure

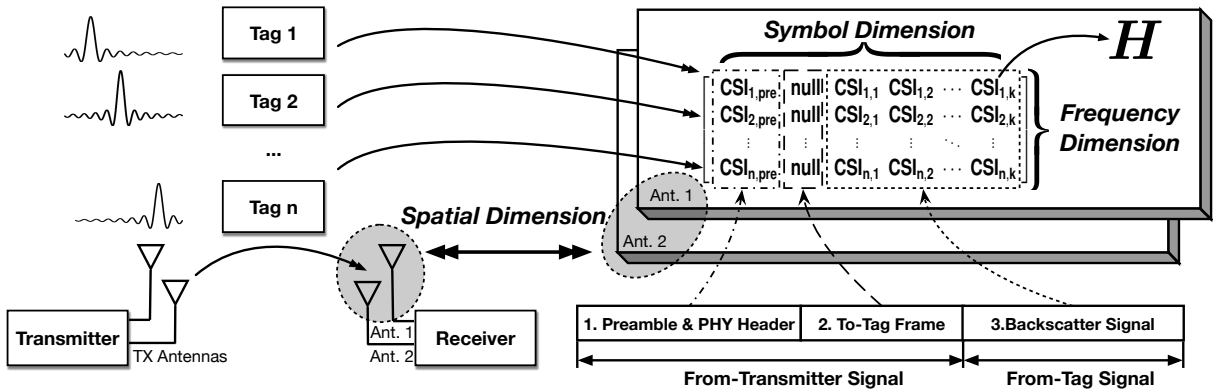


Fig. 4. Concurrent CSI Collection.

accuracy, where signals received at different antennas could be utilized to remove continuous dynamic phase offset.

The frequency dimension represents CSI across different OFDM subcarriers. Since our system assigns different OFDMA subcarriers to different tags, the ID of subcarriers could be utilized to index corresponding tags. As we know, there are 48 data subcarriers in Wi-Fi OFDM systems. Therefore, compared with existing localization methods which can only assign all subcarriers to one certain target, we can assign these subcarriers to 48 targets and therefore collect multi-tag CSI with  $48\times$  efficiency. In this way, we can improve localization concurrency and maintain at most 48 devices communication compared with existing systems.

The symbol dimension represents CSI of different OFDM symbols, which could be utilized to ensure system energy conservation, communication compatibility and accuracy. First, as discussed in *challenge 1*, the synchronization mechanism makes previous packet-level CSI not feasible. However, we regard such a challenge as an opportunity to solve down conversion phase offset problem (*challenge 2*). It is because down conversion phase offset is constant for different propagation paths. Based on symbol dimension information, we can separate from-transmitter CSI and from-tag CSI, which respectively depict channel states of different propagation paths. Since we can simultaneously obtain above information based on one single OFDM burst and then remove down conversion phase offset without extra calibration communication, we realize communication compatibility. Second, for from-tag signals, we can obtain 500 CSI measurements corresponding to 500 OFDM symbols, which provides 500 $\times$  samples compared with prior works. With such fine-grained information, we design the MUSIC extension scheme to improve localization accuracy without sending continuous massive packets in prior works [19, 20, 29], we thus ensure energy conservation and accuracy.

From above contents, we can realize the advantages of 3D-CSI. Here we discuss how to obtain such a fine-grained CSI in our system.

## 4.2 OFDM Burst Processing

As shown in Fig. 4, we first discuss how to acquire symbol-dimension and frequency-dimension CSI matrix at one certain antenna. Then the proposed scheme can be directly applied to the other antennas. In particular, we represent CSI matrix in Fig. 4 as  $H$ . According to the basic knowledge of signals and systems, channel response  $H(f)$  can be derived using the following equation,  $H(f) = S_r(f)/S_t(f)$ , where  $S_r(f)$  and  $S_t(f)$  are respectively frequency-domain descriptions of received signals and transmitted signals. For matrix calculation, we have  $H = S_r./S_t$ , where  $S_r./S_t$  denotes element-by-element division of matrix  $S_r$  and  $S_t$ . Since symbol-dimension

CSI contains three different parts, we calculate them independently. Especially, we represent  $\mathbf{H}$  as a block matrix  $[\mathbf{H}^{pre} \ \mathbf{H}^{null} \ \mathbf{H}^{back}]$ , where  $\mathbf{H}^{pre}$ ,  $\mathbf{H}^{null}$  and  $\mathbf{H}^{back}$  denote CSI of the preamble, to-tag frame and backscatter signals respectively. To calculate this block matrix, we have

$$\mathbf{H} = [\mathbf{H}^{pre} \ \mathbf{H}^{null} \ \mathbf{H}^{back}] = [\mathbf{S}_{rx}^{pre} \ \mathbf{S}_{rx}^{null} \ \mathbf{S}_{rx}^{back}]./[ \mathbf{S}_{tx}^{pre} \ \mathbf{S}_{tx}^{null} \ \mathbf{S}_{tag}^{back}], \quad (1)$$

where  $\mathbf{S}_{rx}^{pre}$ ,  $\mathbf{S}_{rx}^{null}$  and  $\mathbf{S}_{rx}^{back}$  respectively represent the preamble, to-tag frame and backscatter signals at the receiver while  $\mathbf{S}_{tx}^{pre}$ ,  $\mathbf{S}_{tx}^{null}$  and  $\mathbf{S}_{tag}^{back}$  respectively denote these three parts at the transmitter or tags. Among these variables, since the to-tag frame is to coordinate the frequency shift in multiple backscatter tags, they are ignored.

Now we show how to obtain  $\mathbf{S}_{rx}^{pre}$ ,  $\mathbf{S}_{rx}^{back}$ ,  $\mathbf{S}_{tx}^{pre}$  and  $\mathbf{S}_{tag}^{back}$  in our system. First, since the preamble and backscatter signals are captured by the receiver, we can acquire  $\mathbf{S}_{rx}^{pre}$  and  $\mathbf{S}_{rx}^{back}$  via baseband processing in WARP boards. Second, in regular OFDM systems, the transmitter preamble  $\mathbf{S}_{tx}^{pre}$  is known in advance, which is utilized to synchronize the clocks of the transmitter and receiver. Therefore, what we should consider here is how to obtain  $\mathbf{S}_{tag}^{back}$ , which denotes communication information of backscatter signals and is unpredictable. To decode  $\mathbf{S}_{tag}^{back}$ , the most challenge is that there is an unknown phase offset of received backscatter signals, which is caused by unknown channel state. Consequently, we can utilize known information called tag-to-receiver preamble to estimate channel state and then decode backscatter signals with estimated results. In particular, tags embed tag-to-receiver preamble before communication symbols. When the receiver captures backscatter signals, it first estimate channel state with the known tag-to-receiver preamble and then decodes communication symbols. In this way, we can acquire all essential matrices to calculate  $\mathbf{H}$ . *To be stressed that despite the same words utilized, above phase offsets calibration is one necessary communication process and is not equivalent to the phase offsets calibration introduced in challenge 2.* Finally, we process received OFDM signals at different antennas based on the same method and thus derive 3D-CSI. In the following contents of this paper, we employ  $C(m, n, k)$  to denote 3D-CSI, where  $m$ ,  $n$  and  $k$  respectively represent the index of antenna, subcarrier and OFDM symbol. Specifically,  $C(m, n, pre)$  denotes CSI of the transmitter preamble.

In contrast, according to the description in CSI tools [13], packet-level CSI comes from the preamble of the whole OFDM burst, i.e., from-transmitter preamble. In reality, the tag-to-receiver preamble is special in OFDMA backscatter systems and cannot be processed by off-the-shelf CSI tools. Since packet-level CSI only depicts channel state between the transmitter and receiver, it cannot be utilized to localize backscatter tags, which is verified in our experiments in Fig. 11a.

*Remarks:* Section 4 introduces the advantage of our 3D-CSI, where we can ensure concurrency, energy conservation, communication compatibility and accuracy at the same time. Then we process OFDM burst to derive 3D-CSI in OFDMA backscatter systems. The application of OFDMA backscatter in localization systems brings significant promotion to concurrency without nearly performance degradation in other aspects for the following reason. In contrast to OFDM assigning all subcarriers to one single device, OFDMA assigns multiple subcarriers to different devices for concurrent connectivities. Consequently, with multiple devices connected simultaneously, communication capacity of one certain device decreases. However, IoT applications are featured by a large number of devices with short bursts of data, which makes communication capacity of each device less important. Therefore, our system can improve localization concurrency without nearly performance degradation.

## 5 PHASE OFFSET ELIMINATION

The OFDM burst processing module proposed in previous section allows us to acquire 3D-CSI. However, in contrast to packet-level CSI, 3D-CSI suffers even more from phase offsets as discussed in *challenge 2*. In Fig. 5, there are two kinds of phase offsets consisting of continuous dynamic phase offset and down conversion phase

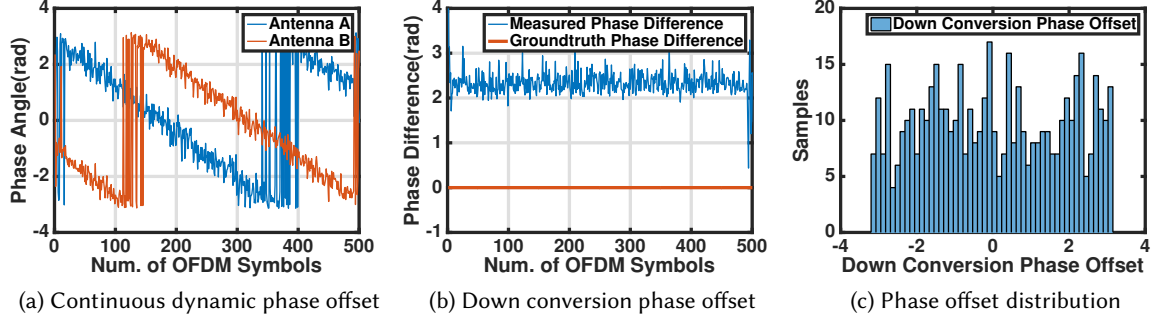


Fig. 5. Phase offset elimination.

offset. This section reveals the root reason for each phase offset and removes phase offsets in real time without previous calibration.

We first represent the phase angle of  $C(m, n, k)$  utilizing  $\varphi_{m,n,k} = \text{angle}(C(m, n, k))$ , which consists of three parts as follows:

$$\varphi_{m,n,k} = \varphi_{m,n,k}^{ex} + \varphi_{m,n,k}^{co} + \varphi_{m,n}^{down}, \quad (2)$$

where  $\varphi_{m,n,k}^{ex}$  denotes the exact phase angle,  $\varphi_{m,n,k}^{co}$  means continuous dynamic phase angle and  $\varphi_{m,n}^{down}$  means down conversion phase angle. Moreover,  $\varphi_{m,n}^{down}$  does not change with the time [8, 12] while the other variables are time-varying.

### 5.1 Continuous Dynamic Phase Offset

As shown in Fig. 5a, we can observe continuous dynamic phase angles at each antenna, which come from the residual frequency offset. In particular, the slopes of phase angles at different antennas are exactly the same i.e.,  $\varphi_{m_1,n,k}^{co} \equiv \varphi_{m_2,n,k}^{co}, \forall m_1, m_2$ . In this way, we can remove continuous dynamic phase offset by calculating phase difference between consecutive antennas and obtain  $\varphi_{\Delta m,n,k} = \varphi_{m_2,n,k} - \varphi_{m_1,n,k} = [\varphi_{m_2,n,k}^{ex} - \varphi_{m_1,n,k}^{ex}] + [\varphi_{m_2,n}^{down} - \varphi_{m_1,n}^{down}]$ . For simplification, we utilize  $\varphi_{\Delta m,n,k}^{ex}$  and  $\varphi_{\Delta m,n}^{down}$  to respectively represent exact phase difference and down conversion phase offsets between consecutive antennas, where  $\varphi_{\Delta m,n,k}^{ex} = \varphi_{m_2,n,k}^{ex} - \varphi_{m_1,n,k}^{ex}$  and  $\varphi_{\Delta m,n}^{down} = \varphi_{m_2,n}^{down} - \varphi_{m_1,n}^{down}$ . We thus have

$$\varphi_{\Delta m,n,k} = \varphi_{\Delta m,n,k}^{ex} + \varphi_{\Delta m,n}^{down}. \quad (3)$$

Continuous dynamic phase offset can be removed without interrupting regular AoA calculation. Review the process of AoA calculation in Fig. 6. The basic idea is when the signals arrive at the antenna array, we can observe a corresponding phase shift at consecutive antennas. Since the distance between the receiver and target is much longer than inter-distance of the antenna array, we can regard propagation paths between target and different antennas as a series of parallel lines. Therefore, in Fig. 6, based on geometric knowledge, we can observe an extra flight distance of the signal at antenna 2 labeled with the red line. It could be written as  $d \sin(\theta)$ , where  $d$  is the distance between consecutive antennas and  $\theta$  is AoA. Then, according to principle of communication, we have corresponding phase shift  $-2\pi \times d \sin(\theta) \times f/c$ , where  $f$  is the frequency of the signal and  $c$  is the speed of

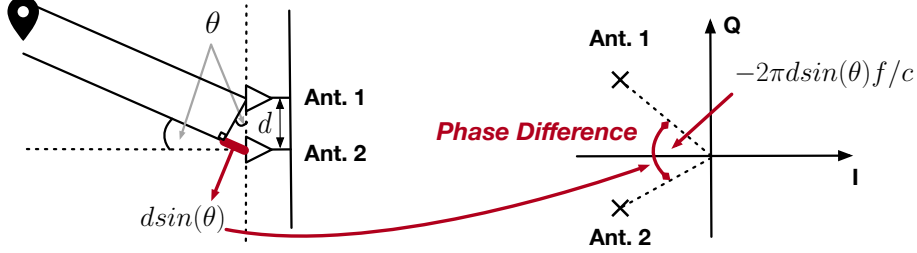


Fig. 6. Relation between AoA and phase difference.

light. Recall the definition of  $\varphi_{\Delta m, n, k}^{ex}$  in Eq. 3, which denotes exact phase angle difference between consecutive antennas caused by extra distance  $d \sin(\theta)$ . Since  $d$  is known in advance, we can derive AoA as follows:

$$\theta(n, k) = \arcsin\left(-\frac{c \times \varphi_{\Delta m, n, k}^{ex}}{2\pi df}\right), \quad (4)$$

where  $\varphi_{\Delta m, n, k}^{ex}$  is necessary to derive AoA and is also maintained after continuous dynamic phase offset elimination. However, by subtracting the phase angle of one antenna from the other antenna, we can just obtain  $\varphi_{\Delta m, n, k}$  in Eq. 3, which consists of two components. Between them,  $\varphi_{\Delta m, n, k}^{ex}$  is what we want for AoA calculation while  $\varphi_{\Delta m, n}^{down}$  is an unknown phase offset caused by down conversion step. In reality, since we can just obtain  $\varphi_{\Delta m, n, k}$  without any other information about its two components, without previous calibration, prior works cannot obtain  $\varphi_{\Delta m, n, k}^{ex}$  for AoA calculation. Especially, prior experiments [12] show that down conversion phase offset might be larger than exact phase difference and leads to an average 60 degrees error of AoA calculation. To address this problem, we now discuss how to remove down conversion phase offsets.

## 5.2 Down Conversion Phase Offset

Fig. 5b shows phase difference between consecutive antennas, where the blue line denotes phase difference  $\varphi_{\Delta m, n, k}$  before down conversion phase offset elimination and the red line denotes exact phase difference  $\varphi_{\Delta m, n, k}^{ex}$ . We can observe a phase offset  $\varphi_{\Delta m, n}^{down}$  between two lines caused by down conversion steps. Though down conversion phase offset doesn't change with the time, it could be reset as a new value once device initializes. We conduct 500 experiments to verify this features and Fig. 5c shows the distribution of down conversion phase offsets, where we can see down conversion phase offsets are exactly random values.

Since down conversion phase offset is an unpredictable value and makes AoA measurement available, existing systems [12] must first calibrate it with dedicated packet transmission. In this section, we propose how to dynamically remove down conversion phase offset without dedicated packet transmission. As shown in Fig. 7, each OFDM burst consists of TX-RX and Tag-RX sub-signals (Part C). For CSI  $C(m, n, pre)$  of the transmitter's preamble, we can also utilize  $\varphi_{m, n, pre} = \text{angle}(C(m, n, pre))$  to denote its phase angle. Calculating phase difference of  $C(m, n, pre)$  between consecutive antennas (Part B), we have

$$\varphi_{\Delta m, n, pre} = \varphi_{\Delta m, n, pre}^{ex} + \varphi_{\Delta m, n, pre}^{down}. \quad (5)$$

where  $\varphi_{\Delta m, n, pre}^{ex}$  denotes exact phase difference (Purple area in part D) and  $\varphi_{\Delta m, n, pre}^{down}$  denotes down conversion phase offset (Gray area in part D). As discussed above, since  $\varphi_{\Delta m, n, pre}^{down}$  is constant for different paths, we have  $\varphi_{\Delta m, n, pre}^{down} \equiv \varphi_{\Delta m, n}^{down}$ . By subtracting  $\varphi_{\Delta m, n, pre}$  in Eq. 5 from  $\varphi_{\Delta m, n, k}$  in Eq. 3, we have  $\varphi_{\Delta m, n, k}^{relative} = \varphi_{\Delta m, n, k} - \varphi_{\Delta m, n, pre} = \varphi_{\Delta m, n, k}^{ex} - \varphi_{\Delta m, n, pre}^{ex}$  (Part E), where  $\varphi_{\Delta m, n, k}^{relative}$  denotes the relative phase offsets of  $n^{th}$  subcarrier

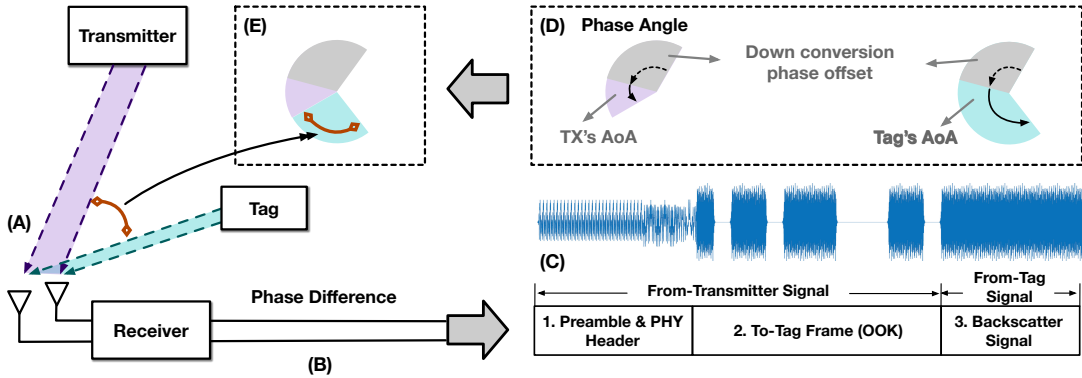


Fig. 7. Down conversion phase offset elimination.

and  $k^{th}$  symbol. From this equation, we can observe that  $\varphi_{\Delta m,n,k}^{relative}$  is composed of  $\varphi_{\Delta m,n,k}^{ex}$  (Blue area in part E) and  $\varphi_{\Delta m,n,pre}^{ex}$  (Purple area in part E), which are corresponding to AoAs of the tag and transmitter respectively. Since position of the transmitter is usually constant and known during localization, we can acquire AoA of the transmitter in advance to determine  $\varphi_{\Delta m,n,pre}^{ex}$  and therefore derive  $\varphi_{\Delta m,n,k}^{ex}$  using

$$\varphi_{\Delta m,n,k}^{ex} = \varphi_{\Delta m,n,k}^{relative} + \varphi_{\Delta m,n,pre}^{ex}. \quad (6)$$

*Remarks:* Section 5 clarifies how to utilize the symbol-dimension information to extract the CSI from different targets and realize the down conversion phase offset elimination without the communication interference. In this section, our system shows three advantages compared with prior works [8, 12, 35]. First, since previous works try to calibrate phase offsets instead of removing it directly like our scheme, they might introduce an extra calibrating error. Second, previous works require special calibration communication, for example, the transmitter sends a message to the receiver to calibrate phase offsets. During their calibration process, multi-tag communication and localization are terminated. In contrast, since the OFDM burst contains both from-transmitter and from-tag signals in our system, we can remove phase offsets while maintaining normal communication and localization. Third, interrupted by environment noise, calibrated results might be inaccurate and re-calibration is necessary to address this problem. Since previous calibration methods cannot work in real time, they request extra performance evaluation to judge calibrated accuracy. In contrast, our system removes phase offsets dynamically, which is more practical and robust.

## 6 EXTENDED MUSIC SCHEME

The phase offset elimination introduced in previous section allows us to remove continuous dynamic phase offset and down conversion phase offset without calibration. To localize targets, recently proposed SpotFi [19] derives accurate AoA based on multiple subcarriers and packets. However, as discussed in *challenge 3*, allocated subcarriers for each target are usually limited in OFDMA backscatter systems and numerous packets would consume much energy. In the following contents, we will first formulate our math model and then reveal why traditional MUSIC schemes and SpotFi cannot provide satisfactory accuracy. Finally, we introduce our extended MUSIC scheme in detail.

## 6.1 Derive AoA of Tags with Limited Information

As shown in Fig. 3, since we perform different extended MUSIC schemes based on the number of subcarriers assigned, we need to establish mapping relationships between tags and subcarriers. For this purpose, we define the subcarrier set of tag  $T$  as  $\mathcal{F}_T$ , which includes all subcarriers assigned to tag  $T$ . For example, supposing that subcarriers #1, #4, #6 are assigned to the tag #2, we have  $\mathcal{F}_2 = \{1, 4, 6\}$ . Then we count the elements of each  $\mathcal{F}_T$  and determine corresponding extended MUSIC scheme.

To derive AoA of tags, we here formulate our math model. Since multiple tags share the same scheme for AoA calculation based on respective subcarrier set, we introduce our extended MUSIC scheme by just discussing a single tag. For each subcarrier, supposing that there are  $L$  paths arriving at the receiver, we can observe  $x_1, x_2, \dots, x_m$  at  $m$  different antennas, which contains the signals coming from  $L$  paths. Meanwhile, as shown in Fig. 6, there is a fixed phase difference  $\varphi^{ex}$  between consecutive antennas. Since signals propagating across different paths arrive at the receiver with different AoAs, we utilize  $\varphi_l^{ex}$  to denote this fixed phase difference corresponding to the AoA of  $l^{th}$  path. If all signals of  $L$  paths arriving at the first antenna could be expressed as  $[s_1, s_2, \dots, s_L]^T$ , we can utilize  $[s_1 e^{\varphi_1^{ex}}, s_2 e^{\varphi_2^{ex}}, \dots, s_L e^{\varphi_L^{ex}}]^T$  to represent the signals at the second antenna. In this way, corresponding signals at the  $m^{th}$  antenna could be denoted by  $[s_1 e^{(m-1)\varphi_1^{ex}}, s_2 e^{(m-1)\varphi_2^{ex}}, \dots, s_L e^{(m-1)\varphi_L^{ex}}]^T$ . Since received signals  $x_m$  observed at the  $m^{th}$  antenna is the combination of multipath signals, we have

$$\begin{bmatrix} x_1 \\ x_2 \\ \vdots \\ x_m \end{bmatrix} = \begin{bmatrix} 1 & 1 & \cdots & 1 \\ e^{\varphi_1^{ex}} & e^{\varphi_2^{ex}} & \cdots & e^{\varphi_L^{ex}} \\ \vdots & \vdots & \ddots & \vdots \\ e^{(m-1)\varphi_1^{ex}} & e^{(m-1)\varphi_2^{ex}} & \cdots & e^{(m-1)\varphi_L^{ex}} \end{bmatrix} \begin{bmatrix} s_1 \\ s_2 \\ \vdots \\ s_L \end{bmatrix} + \begin{bmatrix} n_1 \\ n_2 \\ \vdots \\ n_m \end{bmatrix}, \quad (7)$$

where  $n_m$  denote noise at the  $m^{th}$  antenna while the other variables have been defined. For simplification, we can write Eq. 7 as

$$\mathbf{X} = \mathbf{AS} + \mathbf{N}, \quad (8)$$

where  $\mathbf{X}$  denotes the received signals matrix,  $\mathbf{A}$  is the steering matrix,  $\mathbf{S}$  represents propagation signals of  $L$  paths and  $\mathbf{N}$  is the noise matrix. Especially, each column in the steering matrix  $\mathbf{A}$  is defined as the steering vector that could be written as

$$\vec{\mathbf{a}}(\theta) = [1, \Phi(\theta), \dots, \Phi(\theta)^{m-1}]^T, \quad (9)$$

where  $\Phi(\theta) = e^{\varphi^{ex}} = e^{-j2\pi d \sin(\theta)f/c}$  denotes the phase difference between consecutive antennas. Equation. 8 is the basic expression of MUSIC, which is first proposed in 1986 [27] and widely employed in recent years [12, 19, 29, 35]. The function of MUSIC is to calculate  $\vec{\mathbf{a}}$  with the only knowledge about  $\mathbf{X}$ . Since MUSIC is a common algorithm, we don't discuss its principle in detail here. Instead, we just reveal why MUSIC cannot provide satisfactory accuracy by analyzing how it works. In particular, *to find steering vectors  $\vec{\mathbf{a}}$ , we first calculate the eigenvectors of  $\mathbf{XX}^*$  corresponding to the near-zero eigenvalues, and then compute the steering vectors orthogonal to these eigenvectors*. In reality, for  $M \times 1$  matrix  $\mathbf{X}$ , we can obtain  $M \times M$  matrix  $\mathbf{XX}^*$ . When  $M$  is small, the eigenvectors of  $\mathbf{XX}^*$  is also in low dimension and at most  $M - 1$  eigenvectors could be found corresponding to near-zero eigenvalues. Due to limited number and low dimension, it is difficult to find accurate steering vectors. Since  $M$  denotes the number of antennas and limited antennas could be employed in practical systems, we can see why MUSIC cannot provide satisfactory accuracy.

To address this challenge, SpotFi [19] utilizes multiple subcarriers and packets for accurate localization. However, in OFDMA backscatter systems, multiple subcarriers are assigned to different backscatter tags for concurrent localization while massive packets would lead to insufferable energy consumption and lower localization efficiency.

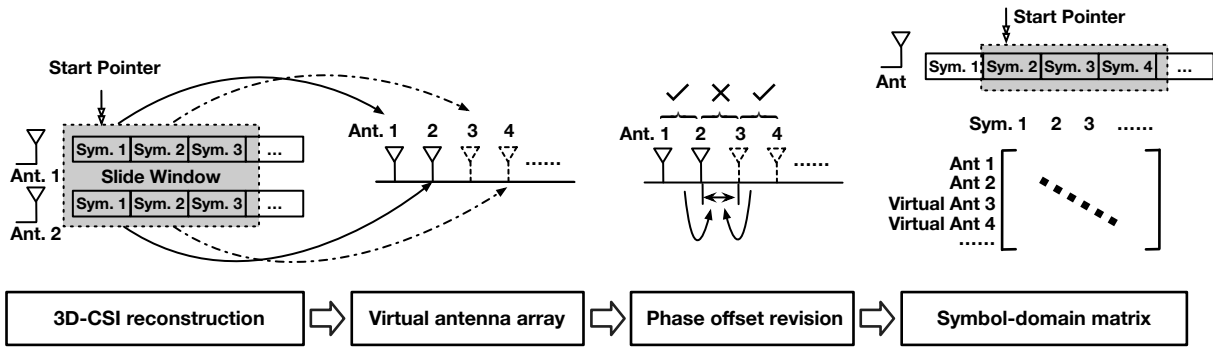


Fig. 8. Symbol-domain extension

Therefore, we here propose extended MUSIC schemes, which consist of symbol-domain extension and multi-domain extension. In particular, symbol-domain extension utilizes symbol-dimension CSI to extend the dimension of  $X$  while multi-domain extension utilizes both symbol-dimension and frequency-dimension CSI. Since symbol-domain extension could be regarded as a specific multi-domain extension where just one subcarrier is available, we first introduce symbol-domain extension and then multi-domain extension.

## 6.2 Symbol-domain Extension

The basic idea of symbol-domain extension is to extend the matrix dimension utilizing 3D-CSI  $C(m, n, k)$ . In particular, as shown in Fig. 8, symbol-domain extension scheme consists of four phases as follows. Here we discuss each phase in detail.

**6.2.1 3D-CSI Reconstruction.** As discussed in §Section 5,  $C(m, n, k)$  is not accurate for AoA calculation due to phase offsets, thus we should reconstruct 3D-CSI based on the exact phase offset  $\varphi_{\Delta m, n, k}^{ex}$  obtained in Eq. 6. From Eq. 4, we can observe that AoA calculation just depends on the phase difference between consecutive antennas. In this way, we can maintain accurate phase difference utilizing the following equation:

$$X(m, n, k) = C(1, n, k)e^{(m-1)\varphi_{\Delta m, n, k}^{ex}}, \quad (10)$$

where  $X(m, n, k)$  is reconstructed 3D-CSI. For the  $n^{th}$  subcarrier,  $X(m, \cdot, k)$  is a  $M \times K$  matrix, where  $M = 2$ ,  $K = 500$  in our system. In contrast, prior works utilize packet-level CSI to localize targets, where they can derive at most  $M \times N$  CSI matrix from each packet. Thus, we can represent packet-level CSI as  $X_{packet}(m, n)$ . In OFDMA backscatter localization, subcarriers assigned to one certain tag are limited, which makes multi-subcarrier CSI unavailable. For one single subcarrier,  $X_{packet}(m, \cdot)$  is reduced to a  $2 \times 1$  matrix. In contrast, our fine-grained CSI can provide a  $2 \times 500$  matrix  $X(m, \cdot, k)$ , which makes extended MUSIC scheme possible. Here, we show how to extend the dimension of  $X(m, n, k)X^*(m, n, k)$  to improve the performance. In particular, supposing that we want to extend the number of rows with  $P$  times as shown in Fig. 8, we can utilize a  $P$ -size slide window to generate symbol-domain extension matrix, denoted by  $X_n^{music}(i, j)$ , where  $i$  is the index of the virtual antenna and  $j$  is start symbol of the slide window. For a given  $P$ , we can finally obtain a  $MP \times (K - P + 1)$  matrix  $X_n^{music}(i, j)$ . In the following contents, we will introduce how to generate such a matrix.

**6.2.2 Virtual Antenna Array.** To generate  $X_n^{music}(i, j)$  mentioned, we first establish the virtual antenna array. As shown in Fig. 8, the basic idea is to pick CSI at different antennas in turn and then put it into a new matrix. For example, we first select  $X(1, n, 1)$  and set it as the first antenna while setting  $X(2, n, 1)$  as the second antenna.

Then we simulate the 3<sup>th</sup> and 4<sup>th</sup> virtual antennas utilizing  $X(1, n, 2)$  and  $X(2, n, 2)$  respectively. And so on, for remaining  $X(m, n, k)$  in the current slide window. Mathematically, we have

$$X_n^{music}(i, 1) = \begin{cases} X(1, n, \frac{i+1}{2}), & i = 2p - 1 \\ X(2, n, \frac{i}{2}), & i = 2p \end{cases}, p \in \mathbb{Z} \text{ and } p < P, \quad (11)$$

where  $p$  denotes the current index. In this way, when the start pointer of the slide window moves to the  $j^{\text{th}}$  symbol, we can summarize the relation between  $X_n^{music}(i, j)$  and  $X(m, n, k)$  as follows:

$$X_n^{music}(i, j) = \begin{cases} X(1, n, \frac{i+2j-1}{2}), & i = 2p - 1 \\ X(2, n, \frac{i+2j-2}{2}), & i = 2p \end{cases}, p \in \mathbb{Z} \text{ and } p < P. \quad (12)$$

According to this equation, we can acquire one  $2P \times (K - P + 1)$  matrix, where  $2P$  denotes the number of virtual antennas while  $(K - P + 1)$  denotes the number of samples. However, such a  $X_n^{music}(i, j)$  cannot be directly utilized for AoA calculation. It is because we can just ensure that partial phase differences between consecutive virtual antennas are exactly correct. In particular, based on Eq. 10, we can just ensure accurate phase offset between  $X(1, n, k)$  and  $X(2, n, k)$  while the one between  $X(2, n, k)$  and  $X(1, n, k + 1)$  is inaccurate. Then we introduce how to revise this inaccurate phase difference.

**6.2.3 Phase Offset Revision.** We employ an interpolation method to address this problem. The basic idea is to revise inaccurate phase difference utilizing adjacent accurate values. For example, for continuous 4 antennas in Fig. 8, we can employ  $\{X_n^{music}(1, j), X_n^{music}(2, j), X_n^{music}(3, j), X_n^{music}(4, j)\}$  to represent them. According to previous discussion, we know that phase difference between  $X_n^{music}(2, j)$  and  $X_n^{music}(3, j)$  is not accurate, denoted by  $\varphi_{\Delta23}$ . In contrast,  $\varphi_{\Delta12}$  and  $\varphi_{\Delta34}$  are accurate, since they both come from the phase difference between  $X(1, n, k)$  and  $X(2, n, k)$ . Therefore, we can employ the mean value of  $\varphi_{\Delta12}$  and  $\varphi_{\Delta34}$  to represent  $\varphi_{\Delta23}$ , where  $\varphi_{\Delta23} = (\varphi_{\Delta12} + \varphi_{\Delta34})/2$ . In this way, we can obtain a modified  $X_n^{music}(i, j)$  to enable the MUSIC algorithm.

**6.2.4 Symbol-domain Matrix for MUSIC..** Previous processes allow us to generate the  $2P \times (K - P + 1)$  matrix  $X_n^{music}(i, j)$  to enable the MUSIC algorithm. Since  $X_n^{music}(i, j)X_n^{music*}(i, j)$  is one  $2P \times 2P$  matrix, compared with  $2 \times 2$  matrix  $X_{packet}(m, \cdot)X_{packet}^*(m, \cdot)$ , the steering vectors calculation suffers less from noise. Meanwhile, since we establish  $2P$  virtual antennas here, the steering vector can be written as  $\vec{a}(\theta) = [1, \Phi(\theta), \dots, \Phi(\theta)^{2P-1}]^T$  according to Eq. 9.

### 6.3 Multi-domain Extension

In OFDMA backscatter systems, it's also possible to assign a group of subcarriers to one certain tag. For feasible multi-subcarrier CSI, SpotFi [19] propose the ToF sanitization algorithm to remove **packet detection delay** [29] via a linear fit of unwrapped multi-subcarrier phase angles. Since the accuracy of linear fit relies on the number of samples, it is difficult to obtain accurate results with limited subcarriers. In this section, we first reveal that the ToF sanitization algorithm is not necessary and cannot improve performance of localization systems. Then we show how to simultaneously perform SpotFi and our symbol-domain extension methods based on discontinuous allocated sub-carriers for more accurate AoA measurement.

**6.3.1 ToF Sanitization Algorithm.** Here we introduce the root reason why ToF sanitization proposed by SpotFi is not necessary in localization systems. Supposing that there are  $L$ -path signals arriving at receiver, ToF of  $l^{\text{th}}$  path is denoted by  $t_l$  while packet detection delay is represented by  $t_{packet}$ . The receiver observes  $s_r(n)$  of  $n^{\text{th}}$

subcarrier, which consists of  $L$ -path signals with respective attenuation  $A_l$  and phase shift  $e^{-j2\pi f t_l}$  caused by ToF  $t_l$ . Besides, there is also an extra phase offset  $e^{-j2\pi f t_{packet}}$  caused by packet detection delay, thus we have

$$s_r(n) = \left( \sum_{l=1}^L A_l e^{-j2\pi f t_l} \right) e^{-j2\pi f t_{packet}}. \quad (13)$$

For  $n^{th}$  subcarrier, its frequency could be denoted by  $f_1 + (n - 1)\Delta f$ , where  $f_1$  is the frequency of the first subcarrier and  $\Delta f$  is the frequency spacing between consecutive subcarriers. Therefore, we can denote the phase shift of  $n^{th}$  subcarrier relative to the first subcarrier as follows:

$$f(n) = \underbrace{\left( \sum_{l=1}^L A_l e^{-j2\pi(n-1)\Delta f t_l} \right)}_{\text{Part A}} \underbrace{\left( e^{-j2\pi(n-1)\Delta f t_{packet}} \right)}_{\text{Part B}}. \quad (14)$$

As we know, the phase angle of complex exponential  $e^{-j2\pi(n-1)\Delta f t_{packet}}$  could be denoted by  $\phi(e^{-j2\pi(n-1)\Delta f t_{packet}}) = -j2\pi(n - 1)\Delta f t_{packet}$ . To remove  $t_{packet}$ , SpotFi tries to deal with the phase shift among different subcarriers via a linear fit. The basic idea is that they first find the best linear fit of  $\phi(f(n))$  and then subtract the phase offset caused by packet detection delay. For example, supposing that  $n$  is the independent variable in equation  $\phi(e^{-j2\pi(n-1)\Delta f t_{packet}}) = -j2\pi(n - 1)\Delta f t_{packet}$ , we can find the best linear fit with a slope  $-j2\pi\Delta f t_{packet}$ . Then we subtract  $-j2\pi n \Delta f t_{packet}$  from  $-j2\pi(n - 1)\Delta f t_{packet}$  and therefore remove packet detection delay. However, we believe such a scheme is not necessary and cannot improve performance of system for the following two reasons:

First, proposed schemes would simultaneously remove parts of ToF information (i.e.,  $t_1, t_2, \dots, t_L$ ) and make ToF inaccurate, which has been verified in their own experiments [19]. The reason is that part A in Eq. 14 also contains linear phase angle components. One simple example is that when there is just one path signal,  $f(n)$  could be represented as  $A_1 e^{-j2\pi(n-1)\Delta f(t_1+t_{packet})}$  and the corresponding phase angle is  $\phi(n) = -j2\pi(n - 1)\Delta f(t_1 + t_{packet})$ . According to the ToF sanitization algorithm, we can obtain the best linear fit  $-j2\pi\Delta f(t_1 + t_{packet})$  and therefore remove both  $t_1$  and  $t_{packet}$ . Since ToF information  $t_1$  has been removed, the ToF sanitization algorithm even leads to worse performance. Furthermore, when there are  $L$  paths, part A contains  $L$  signals with respective linear change. With all multi-path signals summed, the phase angle is dominant by the strongest signal and show linear-like result. Consequently, when removing packet detection delay of part B, the ToF sanitization algorithm still inevitably damage ToF information in part A.

Second, since ToF measured is not accurate, SpotFi just utilizes them to determine the direct path. The basic idea is that the smallest ToF is corresponding to the direct path. In particular, they remove packet detection delay in Eq. 14 and have

$$f'(n) = \left( \sum_{l=1}^L A_l e^{-j2\pi(n-1)\Delta f t_l} \right) e^{-\varphi_{residual}} = \sum_{l=1}^L A_l e^{-j2\pi(n-1)\Delta f t_l - \varphi_{residual}}, \quad (15)$$

where  $\varphi_{residual}$  is the residual phase offset since SpotFi can never obtain the exact packet time delay. Then SpotFi employs the MUSIC scheme to parse a series of ToF, denoted by  $\{t_1 + t_{residual}, t_2 + t_{residual}, \dots, t_L + t_{residual}\}$ , where we can find the direct path  $t_1$  by finding the smallest ToF. In reality, without ToF sanitization algorithm, we can also obtain such a group of ToF, denoted by  $\{t_1 + t_{packet}, t_2 + t_{packet}, \dots, t_L + t_{packet}\}$ , where we still can find the direct path based on the smallest ToF. In conclusion, the ToF sanitization algorithm is not necessary for clear multi-subcarrier information.

**6.3.2 Multi-domain Extension for MUSIC.** In previous section, we show how to establish the symbol-domain extension matrix for MUSIC algorithm. In reality, when a group of subcarriers are assigned to one certain tag, we can utilize both frequency-dimension and symbol-dimension CSI for further performance promotion. The basic idea is to further extend the symbol-domain matrix in Fig. 8 for multi-domain matrix generation. For this purpose, we first determine subcarrier IDs corresponding to current tag. For example, as shown in Fig. 9,

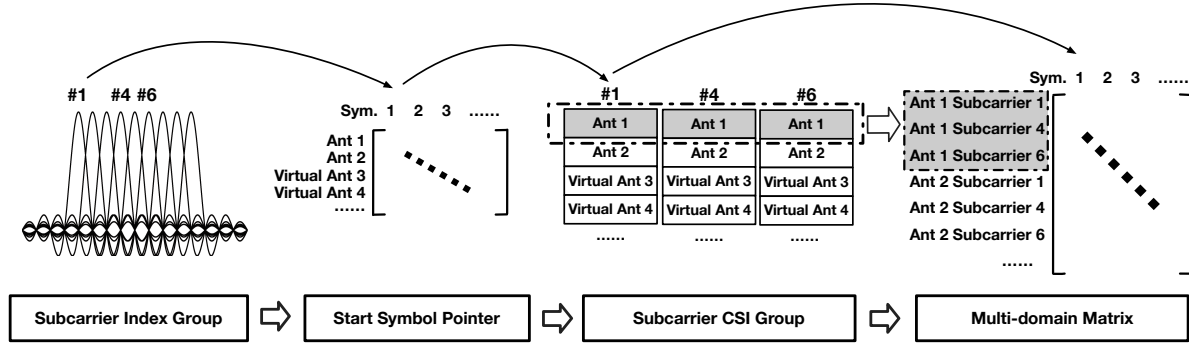


Fig. 9. Multi-domain extension.

supposing that subcarriers #1, #4, #6 are assigned to tag #2, we have  $\mathcal{F}_2 = \{1, 4, 6\}$ . Second, we determine the current start pointer and select corresponding column in the symbol-domain extension matrix. For example, we here select the first start symbol pointer of subcarrier #1, i.e.,  $X_1^{music}(i, 1)$ . Third, for other subcarriers assigned to the same tag, we perform the second step for all assigned subcarriers and obtain subcarrier CSI group, i.e.,  $X_1^{music}(i, 1), X_4^{music}(i, 1), X_6^{music}(i, 1)$ . Finally, we combine different  $X_n^{music}(i, j)$  together utilizing matrix fusion shown in Fig. 9 and therefore obtain the multi-domain extension matrix for MUSIC algorithm.

For MUSIC algorithm, it is necessary to generate steering vector corresponding to the multi-domain extension matrix. In fact, based on subcarrier group and virtual antennas, the steering vector generation is similar to SpotFi [19]. In contrast, our scheme doesn't rely on ToF sanitization algorithm for packet detection delay elimination, which has been proved unnecessary above. Meanwhile, our MUSIC extension scheme is based on limited subcarriers and virtual antennas generated by the symbol-domain extension scheme. Our steering vector, for  $2P$  virtual antennas and  $N$  assigned subcarriers, can be written as

$$\vec{a}(\theta, \tau) = [\underbrace{\Omega_T(1, \tau), \dots, \Omega_T(N, \tau)}_{\text{Antenna 1}}, \underbrace{\Phi(\theta)\Omega_T(1, \tau), \dots, \Phi(\theta)\Omega_T(N, \tau)}_{\text{Antenna 2}}, \underbrace{\Phi(\theta)^{2P-1}\Omega_T(1, \tau), \dots, \Phi(\theta)^{2P-1}\Omega_T(N, \tau)}_{\text{Virtual Antenna } 2P}]^T, \quad (16)$$

where  $\Omega_T(n, \tau) = e^{-j2\pi\mathcal{F}_T(n)f\tau}$  denotes the phase shift caused by different subcarriers while  $\Phi(\theta)$  (Eq. 9) denotes that caused by the antenna array. Inside,  $\mathcal{F}_T(n)$  denotes  $n^{th}$  element in  $\mathcal{F}_T$ . Therefore, we can determine possible  $\tau$  and  $\theta$  utilizing the MUSIC algorithm introduced by SpotFi.

*Remarks:* Section 6 first utilizes symbol-dimension CSI to improve localization accuracy under single-subcarrier scenario and then utilize multi-dimension CSI (i.e. symbol-dimension and frequency-dimension CSI) to further improve localization accuracy under multi-subcarrier scenario. This section provides us with a new solution to address the challenge caused by limited antennas, subcarriers and packets. Compared with previous works which employ multiple antennas, subcarriers and packets for pure performance improvement, we utilize spatial-dimension CSI for phase offset elimination, frequency-dimension CSI for concurrent localization and symbol-dimension CSI to avoid massive packets transmission and maintain accuracy. Therefore, our system provides more practical schemes for concurrent low-power localization systems.

## 7 IMPLEMENTATION AND CONCURRENT LOCALIZATION

We utilize WARP v3 boards [6] to implement the transceiver. Our on-tag transmitter implementation refers to Wi-Fi OFDMA backscatter systems [42]. We utilize some COTS components to realize OFDMA tags by integrating them on an RF-4 PCB board in Fig. 10a. In particular, HMC190BMS8E SPDT switches are employed to change the connection state between receiving and backscattering circuits. To realize SSB signal, which is also described in previous work [40], we use a splitter/combiner BP2U+ [4], ADG902 SPST reflective switch [5] and a printed transmission line.

We utilize DIGILENT NEXYS4 FPGA development boards [2] to control tags communication while using Matlab 2016a to realize OFDM burst processing, phase offsets elimination and extended MUSIC schemes. For every tag localization, at least two AoAs with respect to different receivers are necessary. Since our excitation signal device (WARP v3 board) is full-duplex, it can act as both the transmitter and receiver without any hardware change. In this way, we can derive enough AoAs relative to different transceivers with only one pair of WARP v3 boards.

In this paper, we localize targets based on the following method. In particular, we define an error  $E$  to denote the deviation between AoAs that would be observed at each evaluated location and the corresponding AoAs that were actually observed as follows:

$$E = \sum_{T_1}^{T_N} \sum_{s=1}^S (\bar{\theta}_s(T_n) - \theta_s(T_n))^2, \quad (17)$$

where there are  $S$  receivers and  $T_N$  tags,  $\theta_s(T_n)$  denotes AoA of tag  $T_n$  relative to the  $s^{th}$  receiver while  $\bar{\theta}_s(T_n)$  denotes geometrical AoA of tag  $T_n$  at the  $s^{th}$  receiver corresponding to evaluated position. Finally, we can determine tag's position by finding the minimum  $E$ . Since OFDM subcarriers are orthonormal, each tag localization is independent from the others. Therefore,  $E$  defined in Eq. 17 takes all tags into consideration by directly summing evaluated error of multiple tags.

## 8 EXPERIMENTS

We implement our design on WARP v3 boards and conduct comprehensive experiments in different scenarios to evaluate proposed mechanisms. In our system, each DIGILENT NEXYS4 FPGA development board [2] is utilized to control 4 different backscatter tags. During experiments, we employ 1 ~ 48 tags (40 tags are shown in Fig. 10b) to verify system performance. The position of transceivers and tags can be found in Fig. 10c, where the TX-tag distance is 0 ~ 6m while the tag-RX distance is 0 ~ 6m. To localize backscatter tags, each WARP v3 board is equipped with 2 ~ 4 antennas. We utilize the carton to build NLoS scenarios as shown in Fig. 10d. For multi-tag localization, the transmitter broadcasts necessary wireless signals in channel 2.485GHz.

### 8.1 Necessity of System Designs

We first verify the necessity of our system designs, which consist of three parts corresponding to three challenges. For each experiment, we conduct 500 measurements and compare the results with our proposed scheme.

**8.1.1 Packet-level CSI and 3D-CSI.** Now we are going to verify that 3D-CSI is necessary to address *challenge 1*. As explained in CSI tools [13], since packet-level CSI exactly comes from the preamble of OFDM bursts, we can utilize preamble CSI  $C(m, n, pre)$  to denote packet-level CSI. As shown in Fig. 11a, we can observe that 80% error is within 65 degrees for packet-level CSI localization. Here, we analyze why packet-level CSI is unfeasible. Due to the synchronization mechanism in OFDMA backscatter systems, all OFDM burst preambles come from the transmitter, which denotes that packet-level CSI can just measure channel state between the transmitter and receiver. Since such packet-level CSI can just be utilized to localize the transmitter, we can never derive accurate multi-tag AoAs.

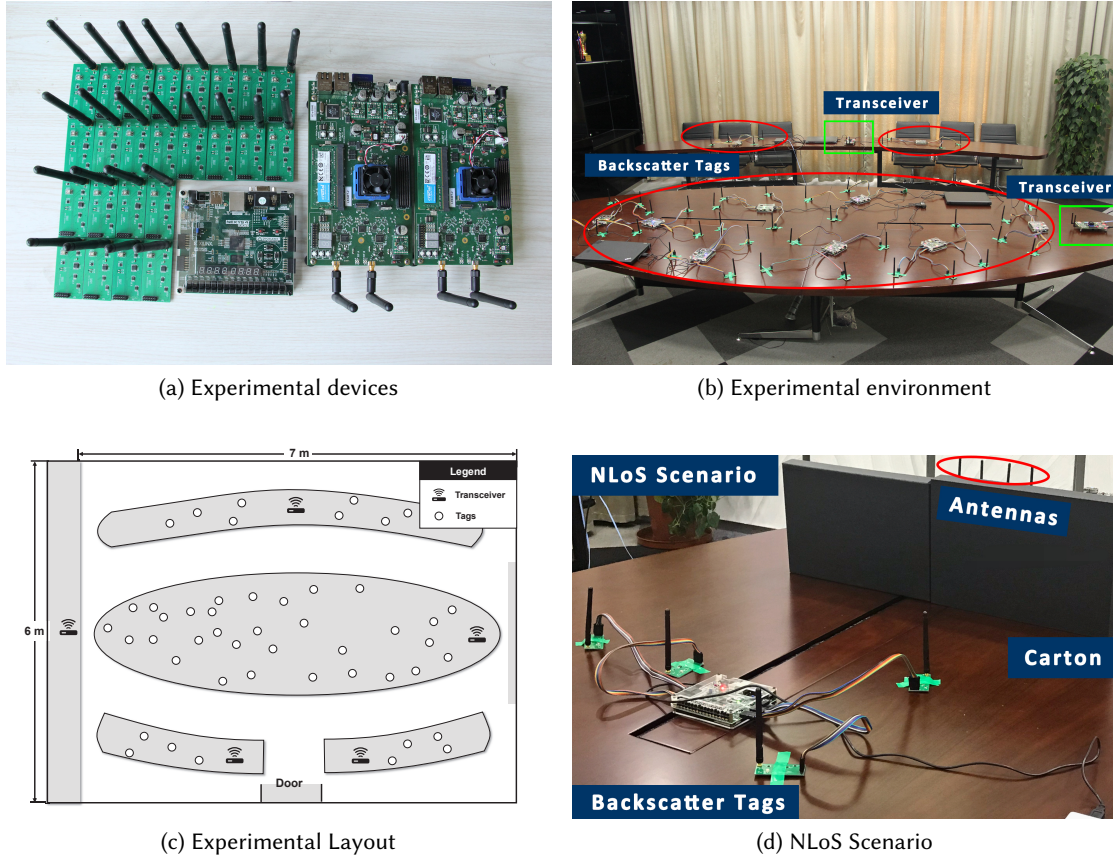


Fig. 10. Groundtruth of the batch localization system. (a) shows experimental devices, where 24 tags, FPGA and WARP v3 boards are presented; (b) shows environment of our experiment in one  $6m \times 7m$  conference room; (c) shows the layout of tags and transceivers; (d) shows how we build the NLoS scenario.

**8.1.2 Phase Offsets Elimination.** To address *challenge 2*, we propose the phase offsets elimination scheme. To realize the necessity of phase offsets elimination, we localize multiple tags with the same data set, where the only difference is whether we remove phase offsets. It can be seen in Fig. 11b that error in degrees is much worse when there is not phase offsets elimination. Thus it is really necessary to remove phase offsets. Similar conclusion has been drawn by ubicarse [21] in Fig. 9, and the underlying reason is as one kind of noise, phase offsets are so large that AoA calculation cannot work.

**8.1.3 MUSIC and Extended MUSIC.** We explain the necessity of the extended MUSIC scheme addressing *challenge 3* by comparing the performance of traditional MUSIC and our scheme. As shown in Fig. 11c, our extended MUSIC scheme realizes half AoA error in degrees compared to the traditional MUSIC scheme. It is because that with limited antennas, subcarriers and packets, existing MUSIC schemes introduced in Eq. 8 are reduced to pure AoA calculation in Eq. 4, which is easily interrupted by noise. For example, we can find that the maximum error is about 120 degrees in contrast to 40 degrees of our extended MUSIC scheme.

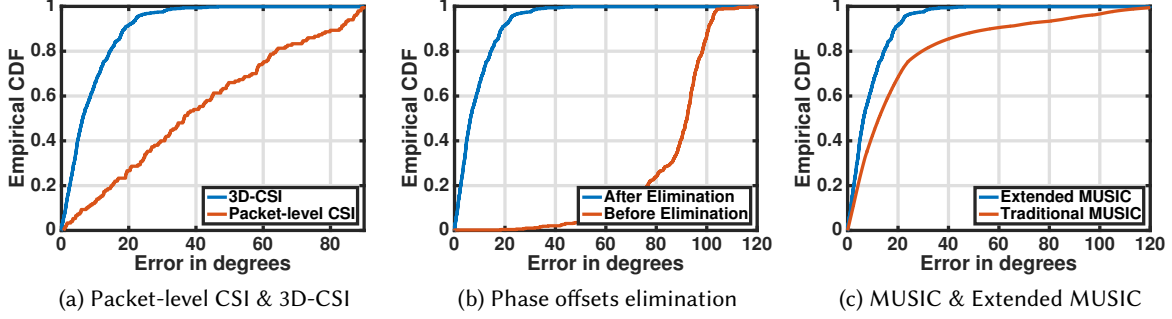


Fig. 11. Necessity of System Designs.

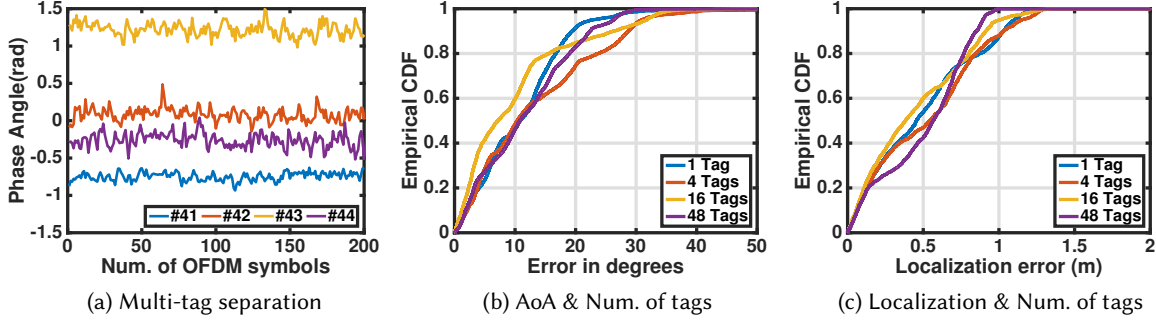


Fig. 12. Localization &amp; Num. of tags

## 8.2 Localization Performance

After verifying the necessity of our system designs, we now comprehensively examine performance of the batch localization system, where the number of backscatter tags, subcarriers and transceivers, experimental scenarios, energy consumption are well considered. We conduct 10 experiments in each situation. Every experiment transmits 50 OFDM bursts and each burst contains 500 symbols. We measure AoA and position according to the information of each OFDM burst.

**8.2.1 The Number of Tags.** To measure the relation between localization accuracy and the number of tags, we respectively employ different numbers of backscatter tags and conduct measurements for different scenarios. We first show how to separate multi-tag AoAs in Fig. 12a, where we plot  $\varphi_{\Delta m, n, k}^{ex}$  (Eq. 6) of different tags. Since  $\varphi_{\Delta m, n, k}^{ex}$  denotes the exact phase difference relative to different AoAs, we can respectively derive AoA corresponding to every tag and therefore separate different tags. For distinct exhibition, we just select 4 different tags and plot  $\varphi_{\Delta m, n, k}^{ex}$  in Fig. 12a, where we can obviously observe that different tags could be separated. Second, we select different numbers of tags (i.e., 1, 4, 16 and 48) to perform our concurrent localization method. The purpose of this experiment is to prove multi-tag localization is feasible in our system. From Fig. 12b, we can observe that with the increase of localized tags, AoA calculation is not interrupted, where the average errors are respectively 11.10, 13.34, 10.02 and 11.71 degrees, the median (90%) errors are respectively 11.10 (19.38), 10.35 (28.66), 7.25 (26.15) and

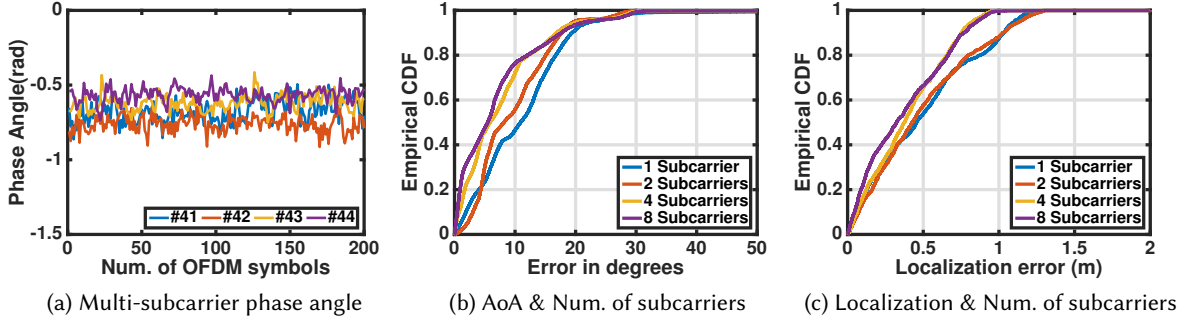


Fig. 13. Localization &amp; Num. of subcarriers

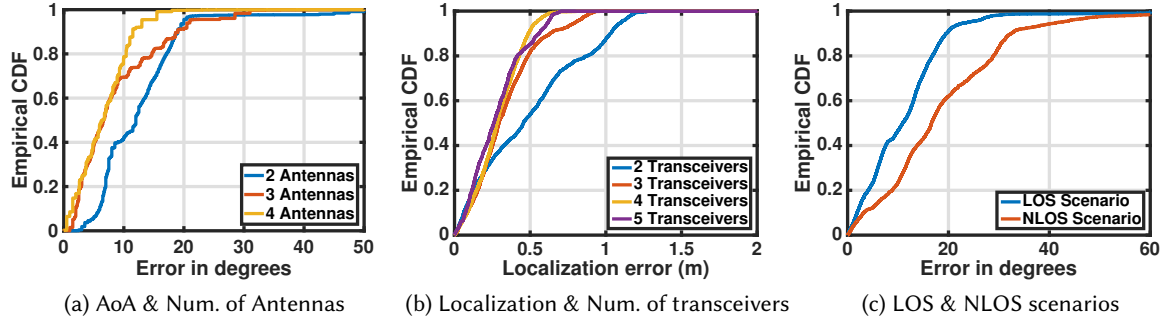


Fig. 14. Localization &amp; Num. of transceivers

10.81 (22.34) degrees. Thus concurrent localization is feasible and doesn't significantly influence localization performance of tags. Third, we utilize derived AoAs to localize multiple tags and therefore obtain localization results shown in Fig. 12c, where we can observe average errors are respectively 0.49m, 0.52m, 0.45m and 0.50m, the median (90%) errors are respectively 0.46m (1.03m), 0.54m (1.03m), 0.37m (0.91m) and 0.56m (0.85m).

**8.2.2 The Number of Subcarriers.** To verify our multi-domain extension scheme, we employ different subcarriers and conduct measurements for different scenarios. We first assign one certain tag multiple subcarriers and plot  $\varphi_{\Delta m, n, k}^{ex}$  (Eq. 6) assigned to this tag. As shown in Fig. 13a, different subcarriers have similar  $\varphi_{\Delta m, n, k}^{ex}$ . It is because that these subcarriers have been assigned to the same tag and are thus corresponding to the same AoA. Second, we select different numbers of subcarriers (i.e., 1, 2, 4 and 8) to perform our extended MUSIC method. As shown in Fig. 13b, with the increase of allocated subcarriers, AoA calculation is improved, where the average errors are respectively 11.10, 9.68, 7.66 and 7.13 degrees, the median (90%) errors are respectively 11.10 (19.38), 9.34 (17.95), 5.82 (17.18) and 5.41 (17.70) degrees. Third, we utilize derived AoAs to localize the tag and therefore obtain localization error shown in Fig. 13c, where we can observe average errors are respectively 0.49m, 0.48m, 0.39m and 0.37m, the median (90%) errors are respectively 0.46m (1.03m), 0.43m (1.03m), 0.38m (0.77m) and 0.33m (0.75m).

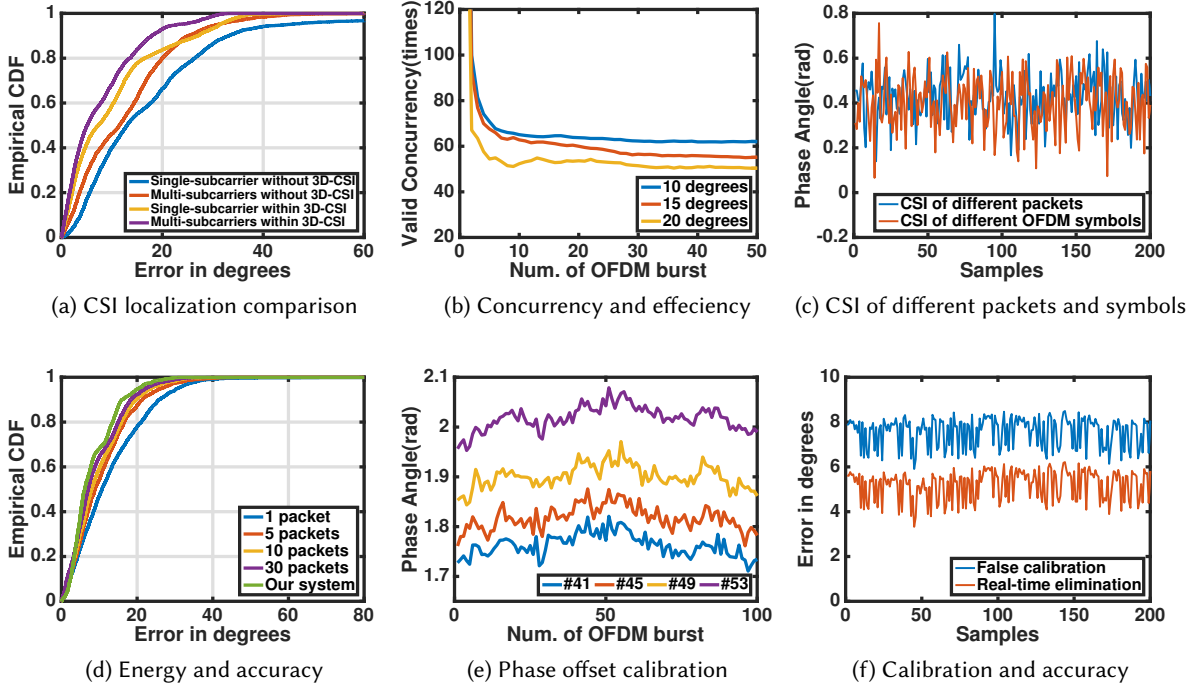


Fig. 15. System Comparison.

**8.2.3 The Number of Antennas.** Since the performance of AoA measurement is dependent on the number of antennas, we conduct experiments with respect to different numbers of antennas. During experiments, we collect CSI and eliminate phase offset based on the method introduced in §Section. 5. With the increase of antennas, we can observe better performance as shown in Fig. 14a, where average errors are respectively 12.48, 8.74 and 6.65 degrees, the median (90%) errors are respectively 12.00 (19.00), 6.60 (19.00) and 6.50 (11.50) degrees.

**8.2.4 The Number of Transceivers.** In batch localization systems, at least two transceivers are necessary to localize multiple tags. During our experiments, we employ different numbers of transceivers to realize batch localization. Since we determine multi-tag position based on AoAs relative to multiple transceivers via Eq. 17, with the increase of transceivers, we can observe better performance in localization as shown in Fig. 14b, where average errors are respectively  $0.49m$ ,  $0.33m$ ,  $0.29m$  and  $0.28m$ , the median (90%) errors are respectively  $0.45m$  ( $1.03m$ ),  $0.30m$  ( $0.63m$ ),  $0.28m$  ( $0.49m$ ) and  $0.26m$  ( $0.56m$ ).

**8.2.5 LoS and NLoS.** To verify system performance under different scenarios, we respectively select LoS and NLoS scenarios to conduct experiments. We conduct measurements for LoS and NLoS scenarios, where average errors are respectively 11.10 and 18.78 degrees, the median (90%) errors are respectively 10.83 (19.38) and 16.65 (32.41) degrees.

**8.2.6 Energy Consumption.** We employ the same tag design as Wi-Fi OFDMA backscatter systems [42], where the overall power consumption of backscatter tag is  $55\text{-}81.3\mu W$ . Here we briefly introduce the energy consumption which consists of the following three parts. The first part comes from the frequency synthesizer realized by

All-Digital PLL whose power consumption is  $0.47\mu W/MHz$ . The second part is the digital part which consumes  $17\mu W$ . Third, we calculate the power consumption of the backscatter circuit by referring to parameters in the datasheets of electronic components. For different switching frequency, the power consumption is  $36.9\text{-}54.4\mu W$ .

### 8.3 Performance Comparison

In this section, we compare our batch localization system with previous methods to verify that we can realize system ***accuracy***, ***concurrency***, ***energy conservation*** and ***communication compatibility*** (§Section. 4). For our scheme, 3D-CSI introduced is available, which is one  $2 \times 48 \times 500$  matrix. As a contrastive scheme, we calibrate phase offsets utilizing the scheme introduced by Phaser [12] and then localize tags one by one via SpotFi [19].

**8.3.1 Accuracy.** To verify the accuracy of our system, we conduct 500 experiments to calculate AoA based on different kinds of CSI and different numbers of subcarriers. During our experiments, single-subcarrier AoA calculation without 3D-CSI is based on the traditional MUSIC scheme [27] while multi-subcarrier AoA calculation is based on the scheme introduced in SpotFi. In Fig. 15a, we can observe average errors are respectively 16.63, 12.66, 10.25 and 7.80 degrees, the median (90%) errors are respectively 13.20 (27.05), 11.35 (25.32), 7.00 (26.80) and 5.05 (17.84) degrees for different kinds of CSI. It denotes that based on one single packet (OFDM burst), we can achieve higher accuracy than existing systems.

**8.3.2 Concurrency and Efficiency.** We conduct 500 experiments to examine the concurrency of our system, where we compare the number of valid localization results in our system with existing works. During our experiments, we respectively regard AoA calculation with error less than 10, 15, 20 degrees are valid. In Fig. 15b, our system shows about  $50\times$  efficiency than existing systems. There are two points to be discussed here. First, we can observe a high multiple at the beginning. It is because that existing works must utilize extra communication to calibrate down conversion phase offset and therefore localize zero tag. Since our system not only removes phase offsets in real time but also has derived multi-tag position, it can get an infinite multiplier here. Second, since we utilize 48 data subcarriers to localize multiple tags, we can realize  $48\times$  concurrency theoretically. In reality, according to Fig. 15b we can realize about 50-65 times efficiency, which is higher than theoretical 48 times. It is rooted in that existing methods show lower accuracy due to coarse-grained CSI shown in Fig. 15a, which denotes that we can derive more valid AoAs and thus realize higher efficiency.

**8.3.3 Energy Conservation.** Our system does not require continuous massive packets for accuracy and therefore ensures energy conservation. Instead, we utilize symbol-dimension CSI and develop extended MUSIC scheme to ensure localization accuracy. During experiments, we first show the phase angle across different packets (OFDM bursts) and OFDM symbols in Fig. 15c, where we can observe the similar results. This experiment shows that it is feasible to replace massive-packet CSI with symbol-dimension CSI. Since we can derive 500 symbol-dimension CSI measurements based on one packet, we ensure energy conservation. Second, we compare energy consumption of our system and existing schemes by analyzing the results based on different numbers of packets (1, 5, 10 and 30). As shown in Fig. 15d, existing schemes require about 30 packets to obtain similar performance as our system, which consumes  $30\times$  energy consequently. Moreover, massive-packet localization proposed in previous works might reduce efficiency further. For example, SpotFi utilizes 10 packets to localize one single tag while our scheme utilizes one single packet to localize 48 tags. Thus our system can finish about 480 times localization while SpotFi just finishes one.

**8.3.4 Communication Compatibility.** Communication compatibility denotes that we do not interrupt other devices' communication when localizing certain targets or calibrating phase offset. As shown in Fig. 13, we can exactly localize multiple tags concurrently. Since available CSI comes from valid communication, we therefore maintain concurrent communication when localizing certain targets. Moreover, our system removes phase offsets

dynamically without special calibration process and therefore ensures communication compatibility. To stress the advantage of our phase offset elimination scheme, we calibrate phase offsets of different OFDM bursts and then plot the results in Fig. 15e. From this figure, we observe that phase offset calibration result is unsteady, which means previous work might derive inaccurate calibration results and therefore obtain inaccurate AoA. For example, in Fig. 15f, false calibration results lead to a higher error in contrast to our real-time calibration.

## 9 RELATED WORK

Ubiquitous employment of IoT devices stimulates the spring-up of indoor localization techniques. Existing works leverage diverse technologies for localization including sound [11, 43], visible light [39] and RF [32–34, 37]. Proposed BatMapper scheme [43] can automatically construct indoor floor plan and realize localization accuracy within 0.3m and LiTell [39] outperforms BatMapper. While these localization systems can provide satisfying accuracy, they usually require dedicated energy-consuming sensors installed in targets such as Wi-Fi, Ultra-wideband (UWB) and Bluetooth chips [32–34, 37] or expensive devices such as mobile phones [11, 39, 43]. However, since IoT devices are usually sensitive to energy, energy-consuming localization sensors limits the development of location-aware applications.

To enable low-power localization, the most innovative method is to localize targets without any installed sensors. With fine-grained CSI available [14], recent researches explore the method of device-free localization and even achieve a better performance than device-based localization [22, 23, 25, 26, 30]. Despite promising accuracy, device-free localization cannot replace device-based localization for the following reasons: First, device-free localization relies on wireless signal reflected by targets, which makes it not applicable for devices in small size. Second, though researches attempt to identify users identities based on people's gait [31, 38], proposed schemes cannot be utilized to identify IoT devices, which do not have gait obviously. Third, device-free localization systems suffer a lot from environment noise and can hardly localize multiple targets.

On the other hand, backscatter technology brings us a new perspective to realize low-power localization, which provides decimeter-level accuracy while constraining power consumption to less than tens of mW. RF-Echo [9] designs an active reflector IC and employs neural networks to estimate ToF. WiTag [20] uses off-the-shelf WiFi chips to localize low-power backscatter tags. However, these researches just provide schemes to localize backscatter tags one by one while concurrent localization remains a challenge. As we know, concurrent transmission would cause collision and make CSI not feasible, thus FreeRider [41] tries to schedule these tags in sequence. Such a method can be similar to the multiple access scheme in commodity RFID systems [24, 41], which is considered to be inefficient [7, 16, 17]. To address this problem, several recently proposed works [15, 42] enable concurrent communication. Despite concurrent communication and CSI collection, existing schemes [9, 20] still cannot be utilized to localize multiple tags concurrently. It is because these schemes require multi-subcarrier CSI coming from the same target for ToF estimation, which is no longer available in concurrent localization systems.

Another problem of CSI localization is that AoA calculation also suffers from an unknown phase offset coming from the down conversion step [8, 12, 21, 35], which leads to inaccurate AoA measurements. To address this problem, previous works [8, 12, 35] require special calibration communication, performance evaluation and re-calibration process, which inevitably interrupts communication of multiple tags.

Our work in this paper solves above challenges and differs from prior works in the following ways: 1) Since previous low-power localization schemes [9, 20] cannot be utilized to localize multiple tags accurately and concurrently, we utilize OFDMA backscatter technology and propose extended MUSIC schemes to enable accurate concurrent localization; 2) In contrast to prior works that try to calibrate phase offsets for accurate localization, our system removes phase offsets in real time without any special calibration process. Thus we realize higher localization accuracy without interrupting communication of any tag.

## 10 CONCLUSION

In this paper, we present how to enable batch localization in OFDMA backscatter. Instead of utilizing multiple antennas, subcarriers and packets for pure accuracy improvement, we appropriately utilize fine-grained CSI to enable system concurrency, energy conservation, communication compatibility and accuracy. First, we utilize frequency-dimension to collect multi-tag CSI concurrently based on OFDMA. Then, we employ spatial-dimension CSI and symbol-dimension CSI to remove phase offsets in real time. Finally, we perform our extended MUSIC scheme and localize multiple tags concurrently. Experimental results show that our system can achieve 50× valid concurrency compared with the existing design. Meanwhile, our system can realize average localization errors within 0.49m while the tag consumes 55–81.3 $\mu$ W active power.

## ACKNOWLEDGMENTS

This work is supported by the National Key Research and Development Program of China 2017YFB1003000, and National Natural Science Foundation of China (No. 61829201, 61872233, 61572319, 61532012).

## REFERENCES

- [1] 2017. Broadcom white paper: 802.11ax: Next generation Wi-Fi for the Gigabit home. Retrieved May 10, 2018 from <https://www.mobileworldlive.com/broadcom-whitepaper-802-11ax-next-generation-wi-fi-for-the-gigabit-home/>
- [2] 2017. FPGA development board, NEXYS4 by DIGILENT. Retrieved May 3, 2018 from <https://reference.digilentinc.com/media/reference/programmable-logic/nexys-4-ddr/nexys4ddrrm.pdf>
- [3] 2017. Introduction to 802.11ax High-Efficiency Wireless-National Instruments. Retrieved May 10, 2018 from <http://www.ni.com/white-paper/53150/en/>
- [4] 2017. Power Splitter/Combiner - Mini Circuits. Retrieved May 3, 2018 from <https://www.minicircuits.com/pdfs/BP2U+.pdf>
- [5] 2017. SPST reflective switch, ADG902 by ADI. Retrieved May 3, 2018 from <http://www.analog.com/media/en/technical-documentation/data-sheets/ADG901902.pdf>
- [6] 2017. WARP: Wireless Open Access Research Platform. Retrieved May 3, 2018 from <http://warpproject.org>
- [7] Omid Abari, Deepak Vasisht, Dina Katabi, and Anantha Chandrakasan. 2015. Caraoke: An e-toll transponder network for smart cities. In *ACM SIGCOMM Computer Communication Review*, Vol. 45. ACM, 297–310.
- [8] Zhe Chen, Zhongmin Li, Xu Zhang, Guorong Zhu, Yuedong Xu, Jie Xiong, and Xin Wang. 2017. AWL: Turning Spatial Aliasing From Foe to Friend for Accurate WiFi Localization. In *Proceedings of the 13th International Conference on emerging Networking EXperiments and Technologies*. ACM, 238–250.
- [9] Li-Xuan Chuo, Zhihong Luo, Dennis Sylvester, David Blaauw, and Hun-Seok Kim. 2017. RF-Echo: A Non-Line-of-Sight Indoor Localization System Using a Low-Power Active RF Reflector ASIC Tag. In *Proceedings of the 23rd Annual International Conference on Mobile Computing and Networking*. ACM, 222–234.
- [10] IEEE Computer Society LAN/MAN Standards Committee et al. 2007. IEEE Standard for Information technology—Telecommunications and information exchange between systems—Local and metropolitan area networks—Specific requirements Part 11: Wireless LAN Medium Access Control (MAC) and Physical Layer (PHY) Specifications. *IEEE Std 802.11* (2007).
- [11] Viktor Erdélyi, Trung-Kien Le, Bobby Bhattacharjee, Peter Druschel, and Nobutaka Ono. 2018. Sonoloc: Scalable positioning of commodity mobile devices. (2018).
- [12] Jon Gjengset, Jie Xiong, Graeme McPhillips, and Kyle Jamieson. 2014. Phaser: Enabling phased array signal processing on commodity WiFi access points. In *Proceedings of the 20th annual international conference on Mobile computing and networking*. ACM, 153–164.
- [13] Daniel Halperin, Wenjun Hu, Anmol Sheth, and David Wetherall. 2010. Linux 802.11 n CSI tool.
- [14] Daniel Halperin, Wenjun Hu, Anmol Sheth, and David Wetherall. 2011. Tool release: Gathering 802.11 n traces with channel state information. *ACM SIGCOMM Computer Communication Review* 41, 1 (2011), 53–53.
- [15] Mehrdad Hessar, Ali Najafi, and Shyamnath Gollakota. 2018. Netscatter: Enabling large-scale backscatter networks. *arXiv preprint arXiv:1808.05195* (2018).
- [16] Pan Hu, Pengyu Zhang, and Deepak Ganesan. 2015. Laissez-faire: Fully asymmetric backscatter communication. In *ACM SIGCOMM Computer Communication Review*, Vol. 45. ACM, 255–267.
- [17] Pan Hu, Pengyu Zhang, and Deepak Ganesan. 2015. Leveraging interleaved signal edges for concurrent backscatter. *ACM SIGMOBILE Mobile Computing and Communications Review* 18, 3 (2015), 26–31.
- [18] Bryce Kellogg, Vamsi Talla, Shyamnath Gollakota, and Joshua R Smith. 2016. Passive WiFi: Bringing Low Power to WiFi Transmissions.. In *NSDI*, Vol. 16. 151–164.

- [19] Manikanta Kotaru, Kiran Joshi, Dinesh Bharadia, and Sachin Katti. 2015. Spotfi: Decimeter level localization using wifi. In *ACM SIGCOMM Computer Communication Review*, Vol. 45. ACM, 269–282.
- [20] Manikanta Kotaru, Pengyu Zhang, and Sachin Katti. 2017. Localizing Low-power Backscatter Tags Using Commodity WiFi. In *Proceedings of the 13th International Conference on emerging Networking EXperiments and Technologies*. ACM, 251–262.
- [21] Swaran Kumar, Stephanie Gil, Dina Katabi, and Daniela Rus. 2014. Accurate indoor localization with zero start-up cost. In *Proceedings of the 20th annual international conference on Mobile computing and networking*. ACM, 483–494.
- [22] Xiang Li, Shengjie Li, Daqing Zhang, Jie Xiong, Yasha Wang, and Hong Mei. 2016. Dynamic-music: accurate device-free indoor localization. In *Proceedings of the 2016 ACM International Joint Conference on Pervasive and Ubiquitous Computing*. ACM, 196–207.
- [23] Xiang Li, Daqing Zhang, Qin Lv, Jie Xiong, Shengjie Li, Yue Zhang, and Hong Mei. 2017. IndoTrack: Device-free indoor human tracking with commodity Wi-Fi. *Proceedings of the ACM on Interactive, Mobile, Wearable and Ubiquitous Technologies* 1, 3 (2017), 72.
- [24] Jiajue Ou, Mo Li, and Yuanqing Zheng. 2015. Come and be served: Parallel decoding for cots rfid tags. In *Proceedings of the 21st Annual International Conference on Mobile Computing and Networking*. ACM, 500–511.
- [25] Kun Qian, Chenshu Wu, Zheng Yang, Yunhao Liu, and Kyle Jamieson. 2017. Widar: Decimeter-level passive tracking via velocity monitoring with commodity Wi-Fi. In *Proceedings of the 18th ACM International Symposium on Mobile Ad Hoc Networking and Computing*. ACM, 6.
- [26] Kun Qian, Chenshu Wu, Yi Zhang, Guidong Zhang, Zheng Yang, and Yunhao Liu. 2018. Widar2. 0: Passive human tracking with a single wi-fi link. *Procs. of ACM MobiSys* (2018).
- [27] Ralph Schmidt. 1986. Multiple emitter location and signal parameter estimation. *IEEE transactions on antennas and propagation* 34, 3 (1986), 276–280.
- [28] Qualcomm Technologies. 2017. 802.11ax: Transforming Wi-Fi to bring unprecedented capacity and efficiency. Retrieved May 10, 2018 from <https://www.qualcomm.com/solutions/networking/features/80211ax>
- [29] Deepak Vasishth, Swaran Kumar, and Dina Katabi. 2016. Decimeter-Level Localization with a Single WiFi Access Point.. In *NSDI*, Vol. 16. 165–178.
- [30] Ju Wang, Hongbo Jiang, Jie Xiong, Kyle Jamieson, Xiaojiang Chen, Dingyi Fang, and Binbin Xie. 2016. LiFS: low human-effort, device-free localization with fine-grained subcarrier information. In *Proceedings of the 22nd Annual International Conference on Mobile Computing and Networking*. ACM, 243–256.
- [31] Wei Wang, Alex X Liu, and Muhammad Shahzad. 2016. Gait recognition using wifi signals. In *Proceedings of the 2016 ACM International Joint Conference on Pervasive and Ubiquitous Computing*. ACM, 363–373.
- [32] Yixin Wang, Qiang Ye, Jie Cheng, and Lei Wang. 2015. RSSI-based bluetooth indoor localization. In *2015 11th International Conference on Mobile Ad-hoc and Sensor Networks (MSN)*. IEEE, 165–171.
- [33] Xudong Wu, Ruofei Shen, Luoyi Fu, Xiaohua Tian, Peng Liu, and Xinbing Wang. 2017. iBILL: Using iBeacon and inertial sensors for accurate indoor localization in large open areas. *IEEE Access* 5 (2017), 14589–14599.
- [34] Jiang Xiao, Zimu Zhou, Youwen Yi, and Lionel M Ni. 2016. A survey on wireless indoor localization from the device perspective. *ACM Computing Surveys (CSUR)* 49, 2 (2016), 25.
- [35] Jie Xiong and Kyle Jamieson. 2013. ArrayTrack: a fine-grained indoor location system. Usenix.
- [36] Jie Xiong, Karthikeyan Sundaresan, and Kyle Jamieson. 2015. Tonetrack: Leveraging frequency-agile radios for time-based indoor wireless localization. In *Proceedings of the 21st Annual International Conference on Mobile Computing and Networking*. ACM, 537–549.
- [37] Zheng Yang, Zimu Zhou, and Yunhao Liu. 2013. From RSSI to CSI: Indoor localization via channel response. *ACM Computing Surveys (CSUR)* 46, 2 (2013), 25.
- [38] Yunze Zeng, Parth H Pathak, and Prasant Mohapatra. 2016. WiWho: wifi-based person identification in smart spaces. In *Proceedings of the 15th International Conference on Information Processing in Sensor Networks*. IEEE Press, 4.
- [39] Chi Zhang and Xinyu Zhang. 2016. LiTell: robust indoor localization using unmodified light fixtures. In *Proceedings of the 22nd Annual International Conference on Mobile Computing and Networking*. ACM, 230–242.
- [40] Pengyu Zhang, Dinesh Bharadia, Kiran Joshi, and Sachin Katti. 2016. Hitchhike: Practical backscatter using commodity wifi. In *Proceedings of the 14th ACM Conference on Embedded Network Sensor Systems CD-ROM*. ACM, 259–271.
- [41] Pengyu Zhang, Colleen Josephson, Dinesh Bharadia, and Sachin Katti. 2017. Freerider: Backscatter communication using commodity radios. In *Proceedings of the 13th International Conference on Emerging Networking EXperiments and Technologies*. ACM, 389–401.
- [42] Renjie Zhao, Fengyuan Zhu, Yuda Feng, Siyuan Peng, Xiaohua Tian, Hui Yu, and Xingbing Wang. 2019. OFDMA-Enabled Wi-Fi Backscatter. In *Proceedings of the 25th Annual International Conference on Mobile Computing and Networking*.
- [43] Bing Zhou, Mohammed Elbadry, Ruipeng Gao, and Fan Ye. 2017. BatMapper: acoustic sensing based indoor floor plan construction using smartphones. In *Proceedings of the 15th Annual International Conference on Mobile Systems, Applications, and Services*. ACM, 42–55.

Received May 2018; revised November 2018; accepted January 2019